


## Granular fluidity in cohesive split-bottom granular flows

Dorian Faroux,<sup>\*</sup> Kimiaki Washino, Takuya Tsuji<sup>✉,†</sup> and Toshitsugu Tanaka  
*Department of Mechanical Engineering, Osaka University, 2-1 Yamada-Oka, Suita, Osaka, Japan*

 (Received 22 March 2022; accepted 11 August 2022; published 31 August 2022)

Despite important progresses in recent continuum modeling, most nonlocal rheologies remain exclusive to dry granular flows. Indeed, popular theories such as nonlocal granular fluidity (NGF) are only valid for dry materials and extensions for wetted particles have yet to be proposed. To address such shortcomings, a detailed analysis of the split-bottom geometry subject to capillary forces is presented. The principal features of such flow are explained and highlighted using a coarse-graining procedure. In particular, the granular fluidity field from the NGF theory is examined and its relationship with the cohesiveness of the material is explored through the dimensionless Bond number. By limiting the scope to critical-state areas and using normalizations based on the granular temperature, exponential-type cohesive constitutive laws have been obtained. This work deepens the current understanding of cohesive granular flows, brings the construction of a cohesive nonlocal rheology one step closer, and leads the way toward a unification of both NGF and kinetic theory frameworks.

DOI: [10.1103/PhysRevFluids.7.084306](https://doi.org/10.1103/PhysRevFluids.7.084306)

### I. INTRODUCTION

Despite the intrinsic complexity of granular materials, numerical modeling of dense granular flows has steadily progressed in the last decade and now provides extremely accurate representations of practical phenomena. Among the latest developments, the inertial rheology [1,2], sometimes referred to as  $\mu(I)$  rheology, has rapidly gained in popularity and is now one of the most commonly used continuum models for the modeling of dense granular flows as shown by its numerous applications [3–5].

However, the inertial rheology is a local theory, and as such, is unable to capture the influence of microscopic interactions on the macroscopic scale manifested by the presence of spatially-dependent nonlocal effects (or grain-size effects) [6,7]. For instance, it has been accepted that the transition between the flowing and static states is not sharp as predicted by the Drucker-Prager criterion of the inertial rheology, but is instead smooth and follows an exponential-type decay [8–11]. Many other manifestations of nonlocality have been observed experimentally, e.g., secondary rheology [12,13], dependency of shear features on the particle size [14–17], arch formation near the nozzle of silos or hoppers [18–20], starting and stopping angles dependency on the granular layer thickness in shallow flows [21,22], etc. To address these issues, local theories have been enhanced to include spatial and particle-size influence in what is usually known as nonlocal models. The Cosserat approach [23,24], the kinetic theory [25], the integral approach [26,27], and the order-parameter models [28–30] constitute the main approaches of nonlocal modeling. In particular, both the order-parameter nonlocal granular fluidity (NGF) model [31,32] and gradient expansion model (GEM) [33] have recently gained in support and have successfully been applied to a wide

---

<sup>\*</sup>dorian@cf.mech.eng.osaka-u.ac.jp

<sup>†</sup>tak@mech.eng.osaka-u.ac.jp

range of geometries [6,34–41] using different numerical implementations [39,42] and have shown similar performances. A similarity between these two models is the presence of a new constitutive variable referred to as *fluidity* which describes the degree of fluidization of the material. Although they share an identical name, the fluidities of each model,  $g$  and  $f$  respectively, are not defined in the same way. The NGF rheology is based on the kinetic elastoplastic theory and quantifies the rate of plastic events while GEM has for foundation the inertial rheology and makes use of the inertial number  $I$  for its fluidity definition. Nonetheless, both fluidities are capable of expressing the variations present in the surroundings thanks to their Laplacian-based expressions and can successfully capture the spatial-dependency of granular materials.

Further studies regarding the microscopic description of the granular fluidity are still ongoing and its expression is continually being made more precise [6,43–45]. At the exception of a recent work from Mandal *et al.* [46], all of these progresses are only valid for dry particles with no bonding forces and cannot be applied to cohesive flows which are nevertheless ubiquitous in the industry. Various cohesive forces can alter the behavior of granular flows, i.e., Van Der Waals interaction [47,48], electrostatic forces [49], or solid bridges [50] but the most represented are definitely the liquid bridges forces occurring in wet flows [51–53]. To expand and benefit from the framework of continuum nonlocal rheologies in cohesive flows, it is essential to study the relation between the granular fluidity and the cohesiveness of the material so that a new meaningful constitutive model can be constructed.

In this work, microscopic data are gathered using discrete element method (DEM) simulations of three-dimensional cohesive split-bottom flows whose surface tension is varied in a range  $\sigma \in [0.01; 0.40]$  N/m. The choice of the split-bottom geometry has been motivated for its complex flow features such as shear-band [17,54], and for its important presence in the literature providing valuable insights [55–58]. The data are then converted into tensorial quantities using a coarse-graining transformation. The obtained variations of macroscopic quantities, and especially the NGF granular fluidity, are finally analyzed to unravel a dependency with the material cohesiveness characterized by the dimensionless Bond number  $Bo$ .

Initially, a description of the NGF rheology and its granular fluidity is given. Then, the DEM framework including the liquid bridge model as well as the choice of optimal parameters for no-slip profiles is presented. The coarse-graining procedure and subsequent results are finally discussed in the last sections.

## II. NGF MODEL AND GRANULAR FLUIDITY

In this work, only the granular fluidity defined by the NGF rheology is considered. The NGF rheology is derived from emulsion theories [59,60]. At first, a purely phenomenological steady-state constitutive model has been proposed by Kamrin and Koval [31]:

$$g = \frac{\dot{\gamma}}{\mu}, \quad (1)$$

$$g = g_{\text{loc}} + \xi^2 \Delta g, \quad (2)$$

where  $\dot{\gamma}$  is the strain rate,  $\mu$  is the stress ratio,  $g$ ,  $g_{\text{loc}}$  and  $\xi$  are the granular fluidity, the local fluidity and the cooperative length, respectively.  $g_{\text{loc}}$  corresponds to the local contribution within the flow, i.e., it is equivalent to the inertial rheology.  $\xi$  is the propagation distance of nonlocalities and is usually of the order of few particle diameters. Their expressions are given by:

$$g_{\text{loc}}(\mu, P) = \begin{cases} \sqrt{P/\rho_s d^2} I_0 \frac{(\mu - \mu_s)}{\mu(\mu_2 - \mu)} & \text{if } \mu > \mu_s, \\ 0 & \text{if } \mu \leq \mu_s, \end{cases} \quad (3)$$

$$\xi(\mu) = A \sqrt{\frac{\mu_2 - \mu}{\Delta\mu |\mu - \mu_s|}} d, \quad (4)$$

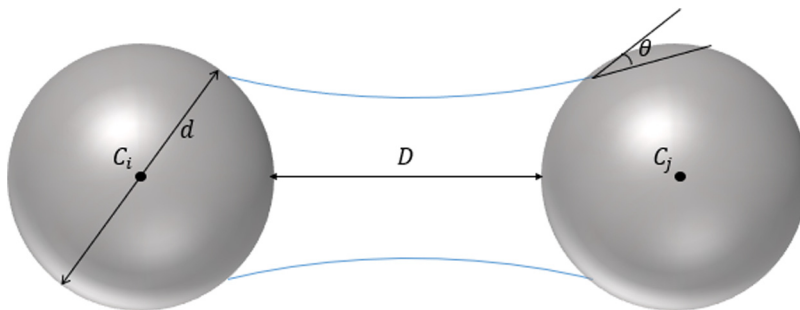


FIG. 1. Illustration of a liquid bridge between two particles.

with  $P$  the pressure,  $\rho_s$  the particle density,  $d$  the particle diameter,  $\mu_s$ ,  $\mu_2$ , and  $I_0$  are material constants derived from the local theory,  $\Delta\mu = \mu_2 - \mu_s$  and  $A$  is a constant dimensionless material parameter commonly referred to as nonlocal amplitude.

In the NGF framework, the granular fluidity  $g$  can be seen as the rate of plastic events. Recent studies have shown that the notion of fluidity holds in microscopic scales and it is dependent on kinematic variables, namely, velocity fluctuations  $V'$ , solid fraction  $\phi$  and particle diameter  $d$  so that  $g = (V'/d)F(\phi)$  [43]. The strong relation between the fluidity and the velocity fluctuations has been further confirmed by the recent discovery of a power-law scaling dependent on the dimensionless granular temperature  $\Theta$  from the kinetic theory [61]. However, such definitions are only valid for dry particles and do not hold for cohesive flows. DEM simulations of cohesive materials are realized to investigate the changes in  $g$  when the capillary forces are present. The entire procedure is described in the following section.

### III. DEM FRAMEWORK

#### A. Capillary force model

In this work, a standard soft-sphere procedure [62] based on the Hertzian [63] and Mindlin [64] models is applied for modeling interparticle interactions. Due to the prevalent use of similar contact models in the literature related to dry particle modeling, and for the sake of brevity, the calculation details have been moved to Appendix A and only the capillary force model will be introduced hereinafter.

The existence of interstitial liquid between particles gives rise to liquid bridges (Fig. 1) and cohesive forces which may alter the behavior of the granular assembly. These bonding forces are usually decomposed into viscous forces which are caused by the relative motion of particles and liquid viscosity, and the capillary forces which are caused by the surface tension [52,53]. For the sake of simplicity, only capillary forces in symmetric pendular bridges are considered in this work.

A liquid bridge, i.e., a bonding force, is created as soon as two particles are located at a distance  $D < D_{\text{rup}}$  from each other, and subsists as long as the distance between the two particles does not exceed the rupture distance  $D > D_{\text{rup}}$ . This assumption is a simplification of the real phenomenon which requires a prior contact between two particles to form a liquid bridge, but does not have a significant influence on the macroscopic behavior. The rupture distance  $D_{\text{rup}}$  has been approximated by Lian *et al.* [65] as

$$D_{\text{rup}} = (1 + 0.5\theta)V_{\text{liq}}^{1/3}, \quad (5)$$

where  $\theta$  is the contact angle and  $V_{\text{liq}}$  is the volume of the liquid bridge. The initial volume of liquid within the granular bed is defined by the saturation

$$S_t = \frac{V_{\text{tot}}}{V_{p\text{tot}}}, \quad (6)$$

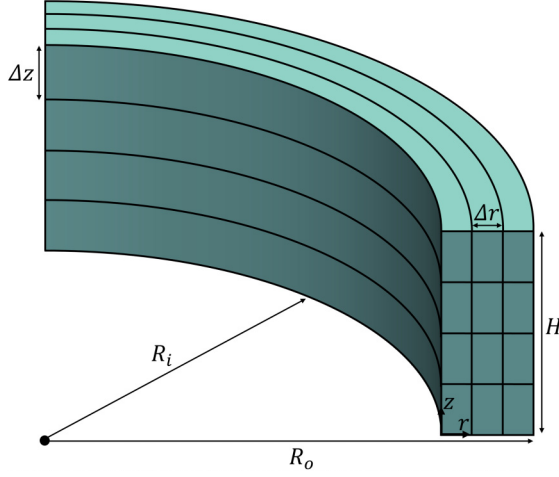


FIG. 2. Illustration of representative volume elements within a 3D annular geometry.

with  $V_{\text{tot}}$  the total volume of liquid and  $V_{p_{\text{tot}}}$  the total volume of particles. Only a portion  $V_{\text{frac}}$  of the total layer of liquid is used for the formation of liquid bridges. Since, both particles are contributing to the creation of the liquid bridge, a factor 2 must be added in the expression of  $V_{\text{liq}}$ :

$$V_{\text{liq}} = 2(4/3)\pi(d/2)^3 S_t V_{\text{frac}}. \quad (7)$$

The proportion  $V_{\text{frac}}$  is arbitrary set to 1/12 which corresponds to a cubic close packing, i.e., the most compact agency for particles. Equation (7) is only valid for the monodisperse case where particles share a same diameter  $d$ . In the case of two particles ( $i, j$ ) of different sizes, the volume becomes

$$V_{\text{liq},ij} = (4/3)\pi((d_j/2)^3 + (d_i/2)^3) S_t V_{\text{frac}}. \quad (8)$$

There are several models available in the literature to calculate the capillary forces of liquid bridges [66–68] with comparable results. In this work, the model proposed by Rabinovich *et al.* [69] which gave reasonable predictions compared with experiments [70] is used. The capillary force for interparticle interactions is given by the following equation:

$$F_{lij}^{p-p} = \frac{4\pi(\bar{d}/2)\sigma \cos \theta}{1 + 1/\left[\sqrt{1 + \frac{V_{\text{liq},ij}}{\pi \bar{r} D^2}} - 1\right]} \mathbf{e}_{nij}, \quad (9)$$

where  $\sigma$  is the surface tension and  $\bar{d} = d_i d_j / (d_i + d_j)$  is the reduced diameter and reduces to  $\bar{d} = d_i/2$  when the particles are of same diameter. To avoid that two pairs of particles give the same maximum capillary force at contact ( $D = 0$ ) for different saturations, i.e.,  $F_{\text{lmax}}^{p-p} = 4\pi(\bar{d}/2)\sigma \cos \theta$ , a minimum distance  $D_{\text{min}}$  is set and defined by the following ratio:

$$R_D = \frac{D_{\text{min}}}{(\bar{d}/2)}, \quad (10)$$

where  $R_D$  is a parameter chosen by the user. The maximum capillary force between two particles thus becomes

$$F_{\text{lmax}}^{p-p} = \frac{4\pi(\bar{d}/2)\sigma \cos \theta}{1 + 1/\left[\sqrt{1 + \frac{V_{\text{liq},ij}}{\pi(\bar{d}/2)D_{\text{min}}^2}} - 1\right]}. \quad (11)$$

In practice,  $R_D$  is chosen so that  $D_{\text{min}}$  is of the order of particle asperities.

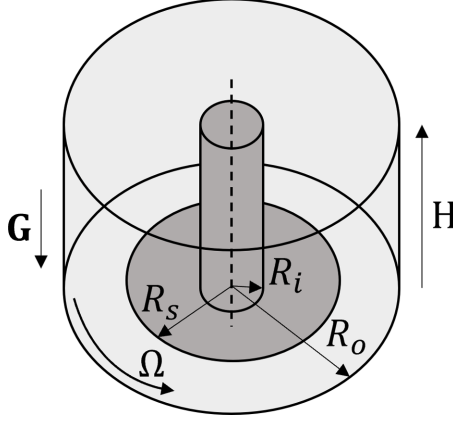


FIG. 3. Split-bottom cell schematics.

The numerical model is finally applied using a velocity Verlet scheme [71] combined with a critical time step  $t_{\text{Ray}}$  based on the propagation time of Rayleigh waves [72]:

$$t_{\text{Ray}} = \frac{f\pi(d/2)}{0.8766 + 0.163\Gamma} \sqrt{\frac{\rho_s}{S}}, \quad (12)$$

where  $f = 0.2$  is a safety factor,  $\Gamma$  is the Poisson ratio of the particles,  $\rho_s$  is the particles density, and  $S$  is the particle shear modulus.

### B. Coarse-graining

The microscopic data obtained from DEM are converted into tensorial quantities compatible with the continuum description through a coarse-graining procedure.

In this work, only cylindrical geometries are considered. Due to the axial symmetry, points at a same distance  $r$  from the center and same height  $z$  are equivalent, i.e., there is no dependency on the angular direction. Therefore, the reference volume elements (RVE) are defined as divisions of the  $r$ - $z$  directions as shown in Fig. 2. The resulting volumes are toroids of width  $\Delta r$  and height  $\Delta z$  so that the volume of one RVE is

$$V_{\text{rve}} = \pi(R_2^2 - R_1^2)\Delta z, \quad (13)$$

where  $R_1$  is the distance from the center of the inner cylinder of the toroid and  $R_2 = R_1 + \Delta r$  is the distance from the center of the outer cylinder of the toroid.

Within each RVE, the microscopic quantities of each particle are subject to both a spatial and temporal averaging. The coarse-graining relations applied in this work are derived from the work of Latzel *et al.* [73] and have subsequently been applied for various 2D and 3D cylindrical geometries [55,56,74–76]. The solid fraction  $\phi$ , the Cauchy stress tensor  $\sigma$  as well as the macroscopic velocity  $V$  are then defined by the following expressions:

$$\phi(r, z) = \frac{1}{\Delta t V_{\text{rve}}} \int_{\Delta t} \sum_{i \in V_{\text{rve}}} V_{p_i} dt, \quad (14)$$

$$\sigma(r, z) = \frac{1}{\Delta t V_{\text{rve}}} \int_{\Delta t} \left( \sum_{i \in V_{\text{rve}}} m_i V'_i \otimes V'_i + \sum_{c \in V_{\text{rve}}}^{\{i,j\}=c} \mathbf{F}_{ij} \otimes \mathbf{l}_{ij} \right) dt, \quad (15)$$

$$\mathbf{V}(r, z) = \frac{1}{\Delta t V_{\text{rve}}} \int_{\Delta t} \left( \sum_{i \in V_{\text{rve}}} V_{p_i} \mathbf{V}_i \right) dt \times \frac{1}{\phi(r)}, \quad (16)$$

TABLE I. Simulation parameters.

Properties	Values
Number of particles $N$	439000
Average particle diameter $d$ [mm]	1.2
Particle density $\rho_s$ [kg/m <sup>3</sup> ]	2450
Height $H$ [mm]	30
Young's modulus $E$ [Pa]	$1 \times 10^8$
Poisson ratio $\Gamma$	0.245
Coefficient of restitution $e$	0.926
Friction coefficient $\mu_p$	0.16
Saturation $S_i$	0.05
Contact angle $\theta$ [deg]	20
Minimum separation distance ratio $R_D$	0.0033
Gravity acceleration $G$ [m/s <sup>2</sup> ]	9.81

with  $V_i$  the velocity of particle  $i$ ,  $V'_i = V_i - \langle V_i \rangle$  the velocity fluctuations where the brackets  $\langle \rangle$  denote the average in the volume  $V_{rve}$ ,  $m_i$  the mass of the particle  $i$ ,  $V_{rve}$  the volume of the RVE,  $V_{p_i}$  the volume of the particle  $i$ ,  $F_{ij}$  the force exerted by  $j$  on  $i$  and  $l_{ij}$  the branch vector between the two particles.

From these variables, a multitude of parameter-fields can be calculated. Using cylindrical coordinates  $(r, \psi, z)$ :

$$\dot{\gamma} = \frac{1}{2} \sqrt{\left( \frac{\partial V_\psi}{\partial r} - \frac{V_\psi}{r} \right)^2 + \left( \frac{\partial V_\psi}{\partial z} \right)^2}, \quad (17)$$

$$|\tau| = \sqrt{\sigma_{r\psi}^2 + \sigma_{z\psi}^2}, \quad (18)$$

$$P = \frac{1}{3} (\sigma_{rr} + \sigma_{\psi\psi} + \sigma_{zz}), \quad (19)$$

$$\eta = \frac{|\tau|}{\dot{\gamma}}, \quad (20)$$

$$\mu = \frac{|\tau|}{P}, \quad (21)$$

$$g = \frac{\dot{\gamma}}{\mu}, \quad (22)$$

where  $\dot{\gamma}$  is the strain rate,  $\tau$  is the shear stress,  $P$  is the pressure,  $\eta$  is the viscosity,  $\mu$  is the stress ratio and  $g$  is the granular fluidity. The gradients in Eq. (17) are computed using a central differencing scheme so that

$$\frac{\partial V_\psi^S}{\partial r} = \frac{V_\psi^{S+1} - V_\psi^{S-1}}{2\Delta r}, \quad (23)$$

$$\frac{\partial V_\psi^S}{\partial z} = \frac{V_\psi^{S+1} - V_\psi^{S-1}}{2\Delta z}, \quad (24)$$

with  $S$  the index of the targeted RVE.

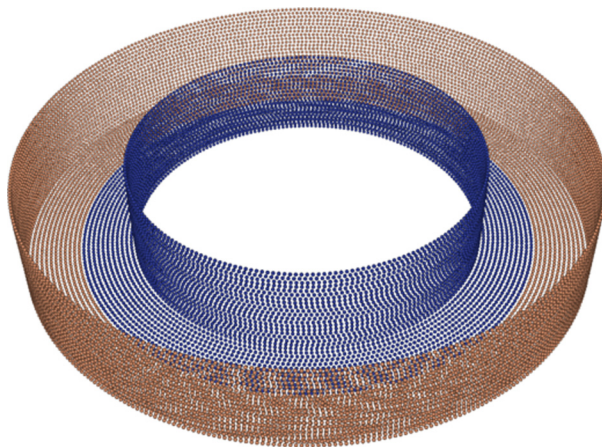


FIG. 4. Walls of a split-bottom cell made of glued particles.

## IV. PREPARATION OF DEM SIMULATIONS

### A. Geometry

The geometry chosen in this work is the split-bottom cell which presents complex shearing features and is a popular reference case for the study of cohesive flows [56,77]. The details are given in Fig. 3.

The static inner part of the cell is composed of the central cylinder of radius  $R_i = 65$  mm and a disk of radius  $R_s = 85$  mm while the outer wall  $R_o = 105$  mm and the external bottom area are rotated at a fixed angular velocity  $\Omega = 0.16$  rad/s. The granular material is then dragged by the fully rough walls and is sheared at the junction between the stationary and moving sections. The internal field is composed of polydisperse glass beads whose distribution follows a Gaussian centered on  $d = 1.2$  mm to avoid crystallization. The beads quantity has been chosen to obtain an initial solid fraction  $\phi_o$  of approximately 0.6. The Young's modulus of glass beads has been lowered to save calculation time while keeping a value high enough to avoid any alteration of the flow field. The simulations parameters are summarized in Table I.

To obtain meaningful comparisons with experiments or continuum modeling, it is necessary to set the boundary conditions of the DEM domain appropriately. The top surface is let free and no specific constraints are imposed at the free-surface. For the walls, however, a no-slip boundary corresponding to rough walls must be implemented. While it is straightforward in continuum modeling, it is less trivial to achieve in a DEM framework. One solution to simulate no-slip surface is to use baffles [78,79]. This solution has the advantage of being simple to implement but may lead to strong wall effects. To obtain a less disturbed flow field closer to real physical systems, walls made of particles are used to replicate a layer of particles glued to the boundary [80]. An example is given in Fig. 4.

With this method, the roughness of the walls is dependent on the spacing and sizes of the glued particles. The notion of roughness factor is used for the parametrization of the wall-particles [81]

$$R_f = \frac{L_p}{d_{w-p}}, \quad (25)$$

with  $L_p$  the distance between two particles (Fig. 5). If the particles are too far from each other, or on the contrary too close, then they might form a nearly-smooth layer of particles on top of which particles from the internal field can slip.  $R_f = 0.5$  is kept in this work. Moreover, it is ensured that no particle can go through the gaps by adding solid walls behind the wall-particles as shown in Fig. 6. For a small roughness factor value, these additional safety walls are optional since the interstices

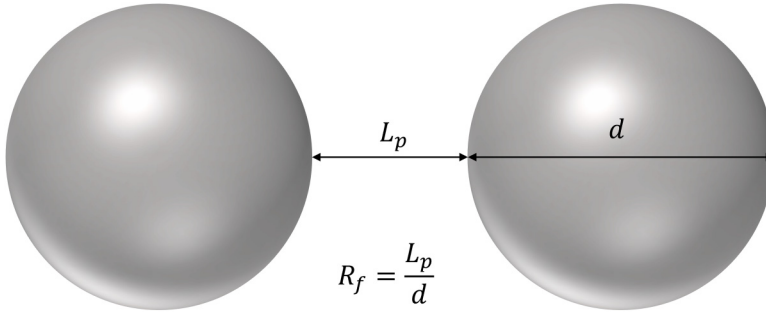


FIG. 5. Roughness factor based on the interparticle space and particle diameter.

between the particles is too small to let any escape. In our case, three walls are implemented, one for the inner cylinder, one for the outer cylinder, and one for the bottom. The distance  $D_{pl}$  separating the walls from the center of the particles may have an influence on the wall boundary behavior and must also be chosen carefully. In this work,  $D_{pl} = 0.559$  mm is chosen. Details regarding the determination of optimal values for  $R_f$  and  $D_{pl}$  are given in Appendix B.

All the wall-particles of the simulations presented in this work have the same properties as the internal particles. Therefore, they are characterized by a diameter  $d_{w-p} = 1.2$  mm and can also be involved in the formation of liquid bridges with neighbors particles.

### B. Coarse-graining parameters

Granular materials are nonlocal both in time and in space, i.e., there is no clear separation of scale between the micro and macroscales and time fluctuations are present [82–84]. Therefore, the choice of RVE (Fig. 2) as well as the time step between snapshots can have an observable influence on the resulting macroscopic fields.

For three-dimensional annular geometries, it is common to choose an arbitrary volume whose dimensions  $\Delta r \times \Delta z$  are of the order of the average particle diameter  $d$  [56,74,75], where no visible changes are noticed in the  $1 - 5d$  range. A similar behavior has been observed in this work, both  $\Delta r$  and  $\Delta z$  are arbitrarily chosen to be 2.5 mm. Regarding the temporal averaging, only the later steady-state snapshots  $10 < t < 15$  s are used with a time step of  $\Delta t = 0.1$  s, i.e., 50 snapshots. Due to the short simulation time considered here, it is not excluded that long-time relaxation effects may have a slight influence on our findings.

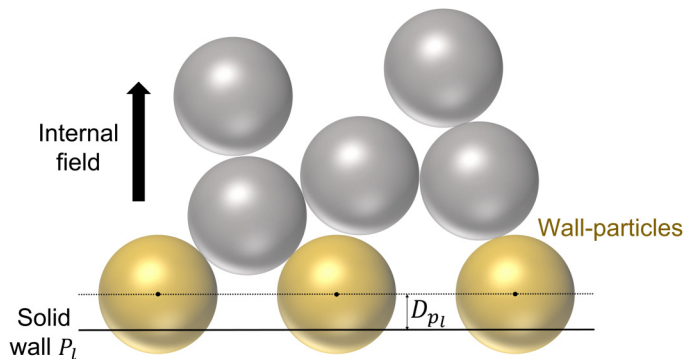


FIG. 6. Safety walls  $P_l$  to prevent the passage of internal particles between the wall-particles.



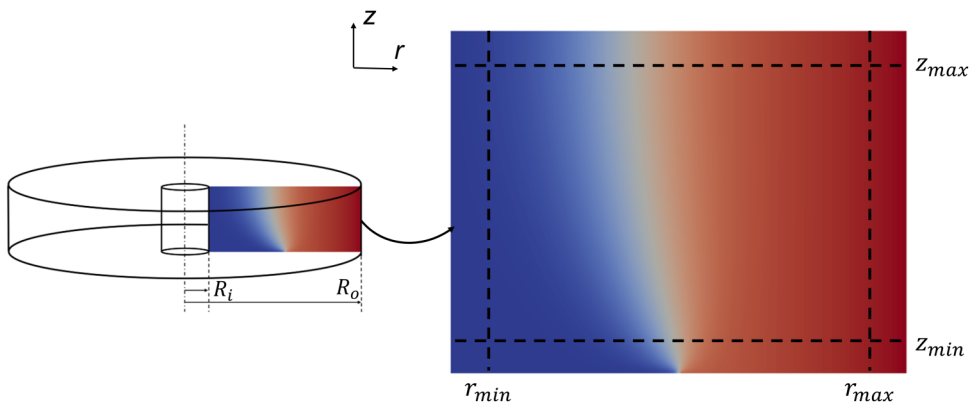


FIG. 7. Spatial limits of the coarse-graining domain.

Finally, the domain in which the coarse-graining procedure is applied is limited to avoid any wall effects. Figure 7 displays a section  $r$ - $z$  within the split-bottom cell. The micro-macro transition is then realized between the limits  $(r_{\min}, r_{\max})$  and  $(z_{\min}, z_{\max})$ .

For the current geometry:

$$\begin{aligned} r_{\min} &= 66 \text{ mm} & \text{and} & & r_{\max} &= 104 \text{ mm}, \\ z_{\min} &= 1 \text{ mm} & \text{and} & & z_{\max} &= 29 \text{ mm}, \end{aligned} \quad (26)$$

written in terms of particle diameter:

$$\begin{aligned} r_{\min}/d &= 55 & \text{and} & & r_{\max}/d &= 86.7, \\ z_{\min}/d &= 0.8 & \text{and} & & z_{\max}/d &= 24.2. \end{aligned} \quad (27)$$

## V. COHESIVE SPLIT-BOTTOM FLOWS

### A. Qualitative flow fields

With the purpose of uncovering the physics of nonlocal granular flows under the influence of bonding forces, the aforementioned DEM procedure is applied to the split-bottom geometry in which capillary forces are present. To obtain a large span of flow regimes, a wide range of surface tensions is explored:  $\sigma \in \{0.01, 0.02, 0.04, 0.07, 0.10, 0.15, 0.20, 0.25, 0.30, 0.35, 0.40\}$  [N/m].

The steady-state coarse-grained quantities are plotted in the  $z$ - $r$  plane and the evolution of the split-bottom flow physics for increasing surface tensions is analyzed. The first tensorial field to be examined is the velocity field as shown in Fig. 8. For ease of visualization, the steady-state profiles of each case are gathered in a single figure and the color scales are kept identical through each plot. Both a widening of the shear band and an inward displacement of its center are observed for medium values of surface tension, i.e.,  $\sigma \in [0.07, 0.10, 0.15]$  N/m. Such behavior is in agreement with observations from experiments [16,54] and with predictions from theoretical models [55,85]. In particular, the  $\sigma = 0.15$  N/m case presents a large central area where the velocity is barely evolving and remains quasiuniform. The center of the shear band is not distinguishable anymore, the majority of the domain moves as a single body. Simultaneously, a general decrease of the velocity is noticed in the entire domain. The wall velocity  $V_{\text{wall}} = R_o\Omega = 0.0168$  m/s is not reached for  $\sigma \geq 0.07$  N/m cases, highlighting a slip effect at the outer rotating wall. The velocity keeps decreasing until reaching near-zero values in the whole cell. This behavior is due to the strong capillary forces which reinforces the solid-like behavior of the internal particles and form clusters of particles, more difficult to put in motion. In the most extreme cases, i.e.,  $\sigma \in [0.35, 0.40]$  N/m, the outer wall-

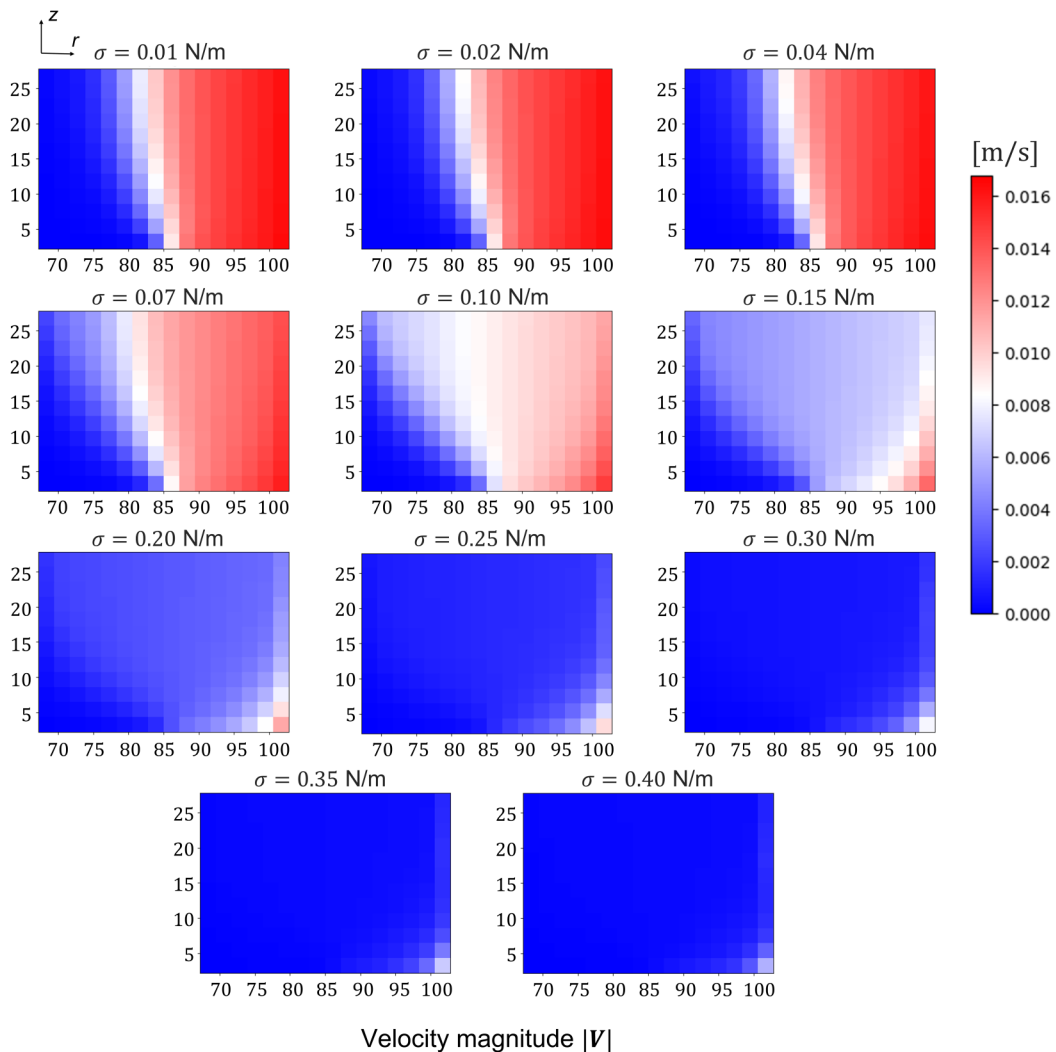


FIG. 8. Coarse-grained velocity in a cohesive split-bottom cell for different values of surface tension  $\sigma$  and a rotational rate  $\Omega = 0.16$  rad/s.

particles simply slide on the internal particles without being able to break the cohesive bonds and drag them. As a result, the shear band is now located in the vicinity of the moving outer walls.

The aforementioned observations are confirmed and emphasized by the volume fraction snapshots given in Fig. 9. The volume shows a clear demarcation between the dilated and compressed regions as the surface tension increases. Notably, an important dense cluster with high  $\phi$  values starts forming for  $\sigma \in [0.10, 0.15]$ . This cluster is then sharpened for higher cases. For  $\sigma = 0.40$  N/m, the contrast is maximum and a dilated area appears underneath the dense cluster. This difference in volume fraction is the manifestation of sheared regions. Indeed, from  $\sigma = 0.10$  N/m, we observe a split of the central shear band into two side parts: one on the left and one on the right. These two parts are simply the extremities of the wide shear band displayed in the previous velocity profiles. Since the central region acts more like a uniform solid due to the bonding forces, it is less likely to be sheared than the sides. Besides, it has been shown in the literature [86] that a dilation of granular matter is expected in sheared areas, hence the current pattern. Cohesion leads

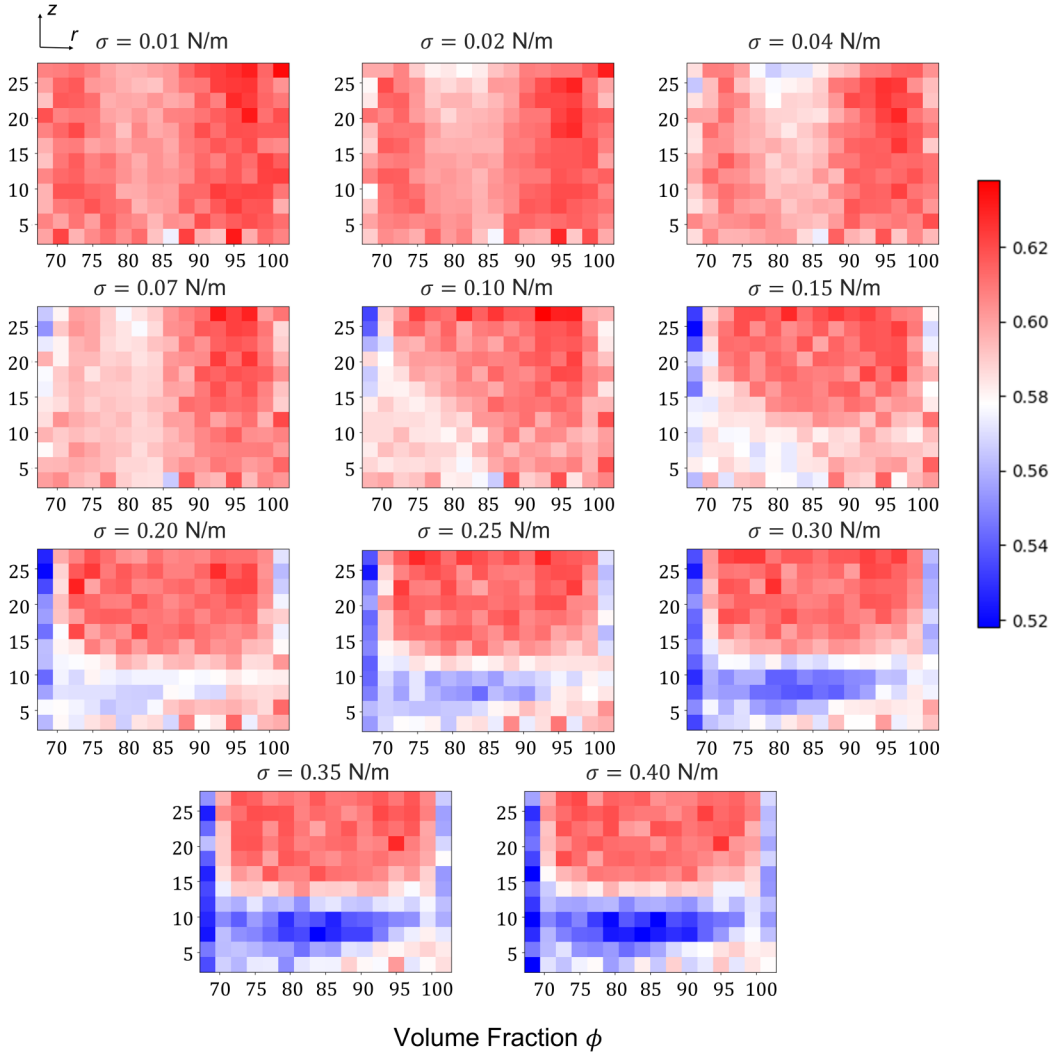


FIG. 9. Coarse-grained volume fraction in a cohesive split-bottom cell for different values of surface tension  $\sigma$  and a rotational rate  $\Omega = 0.16$  rad/s.

to greater heterogeneity and questions the validity of incompressible continuum rheologies which usually assume a uniform solid fraction through the granular phase.

Due to the strong relation between the strain rate and the granular fluidity, it is without surprise that the  $g$  profiles follow similar changes to the strain rate ones (Appendix C) as displayed in Fig 10. From a microscopic perspective, these plots confirm that the plastic events and velocity fluctuations are mainly localized within the shear bands, and that their magnitude decreases with the strengthening of liquid bonds. The liquid bridges between particles prevent the individual particles to move freely in their vicinity and firmly fix them in place. Now, by interpreting the granular fluidity as a degree of fluidization, it is physically consistent that the peak values are distributed in the highly sheared areas while the remaining domain is subject to slow creeping flows with low  $g$  values. Finally, both the strain rate and fluidity snapshots bring out an additional characteristic of cohesive flows. The higher the surface tension, i.e., the stronger the cohesive effects, the thinner the interface between the static and flowing areas becomes. Indeed, the shear band in  $\sigma \in [0.10, 0.15]$

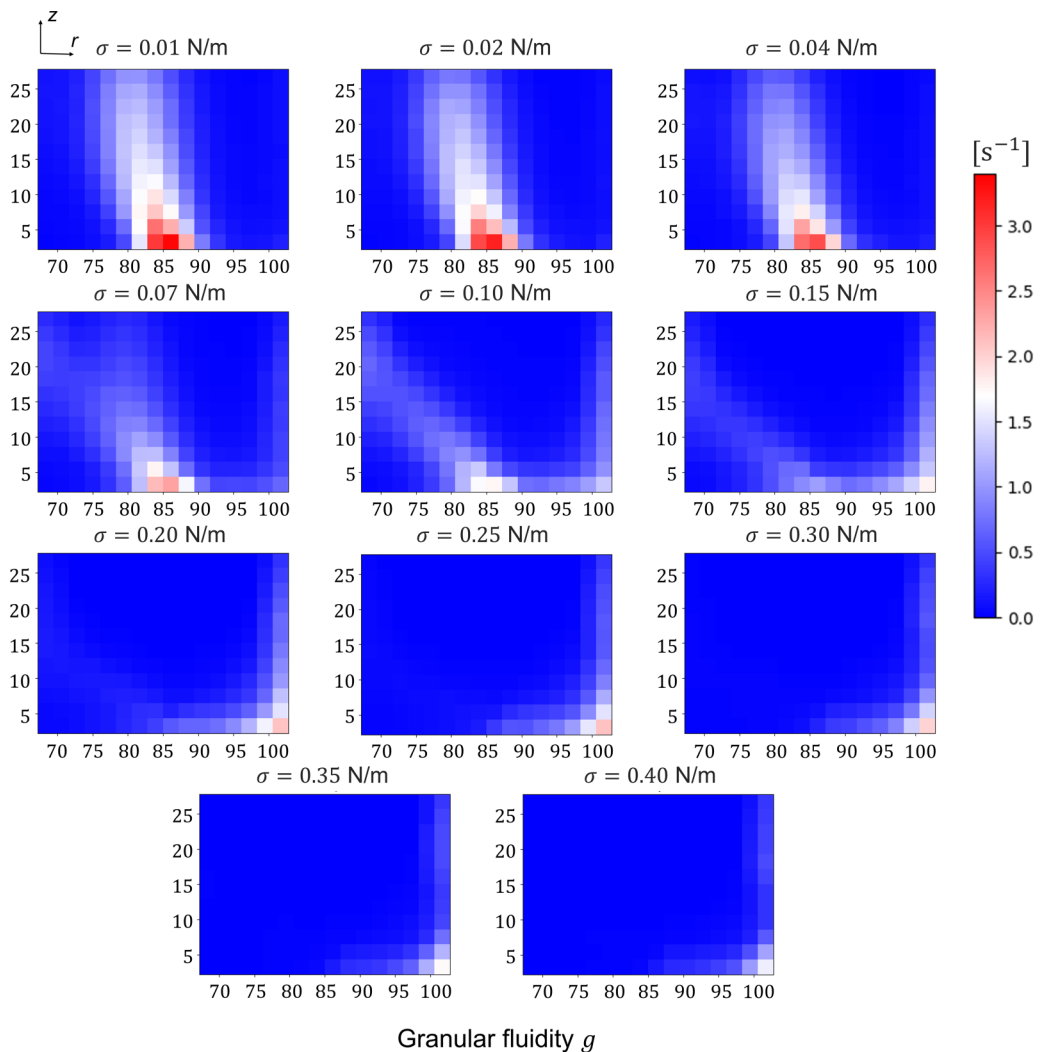


FIG. 10. Coarse-grained granular fluidity in a cohesive split-bottom cell for different values of surface tension  $\sigma$  and a rotational rate  $\Omega = 0.16$  rad/s.

N/m cases is significantly sharper than for the  $\sigma \in [0.01, 0.02, 0.04]$  plots. Instead of having a smooth transition between the different states as observed in dry granular flows, the material is now acting closer to a crystal-like solid whose dislocation line is represented by the narrow shear band, allowing slip-type behaviors between the disconnected layers.

A new macroscopic quantity quantifying the cohesiveness of the materials is then introduced: the bond number  $\text{Bo}$ . The bond number represents the ratio of the maximum attractive force to a typical force scale in the system. Many alternatives have been proposed in the literature regarding the choice of the representative force in the system, e.g., gravity [87], mean force per contact [77], or confining pressure [56,88]. In this work, the cohesiveness of the granular material is expressed using the average force induced by the local confining pressure:

$$\text{Bo} = \frac{F_{\text{lmax}}^{p-p}}{Pd^2}, \quad (28)$$

where  $F_{\text{lmax}}^{p-p}$  is the maximum liquid bridge force for two close particles defined by Eq. (11).

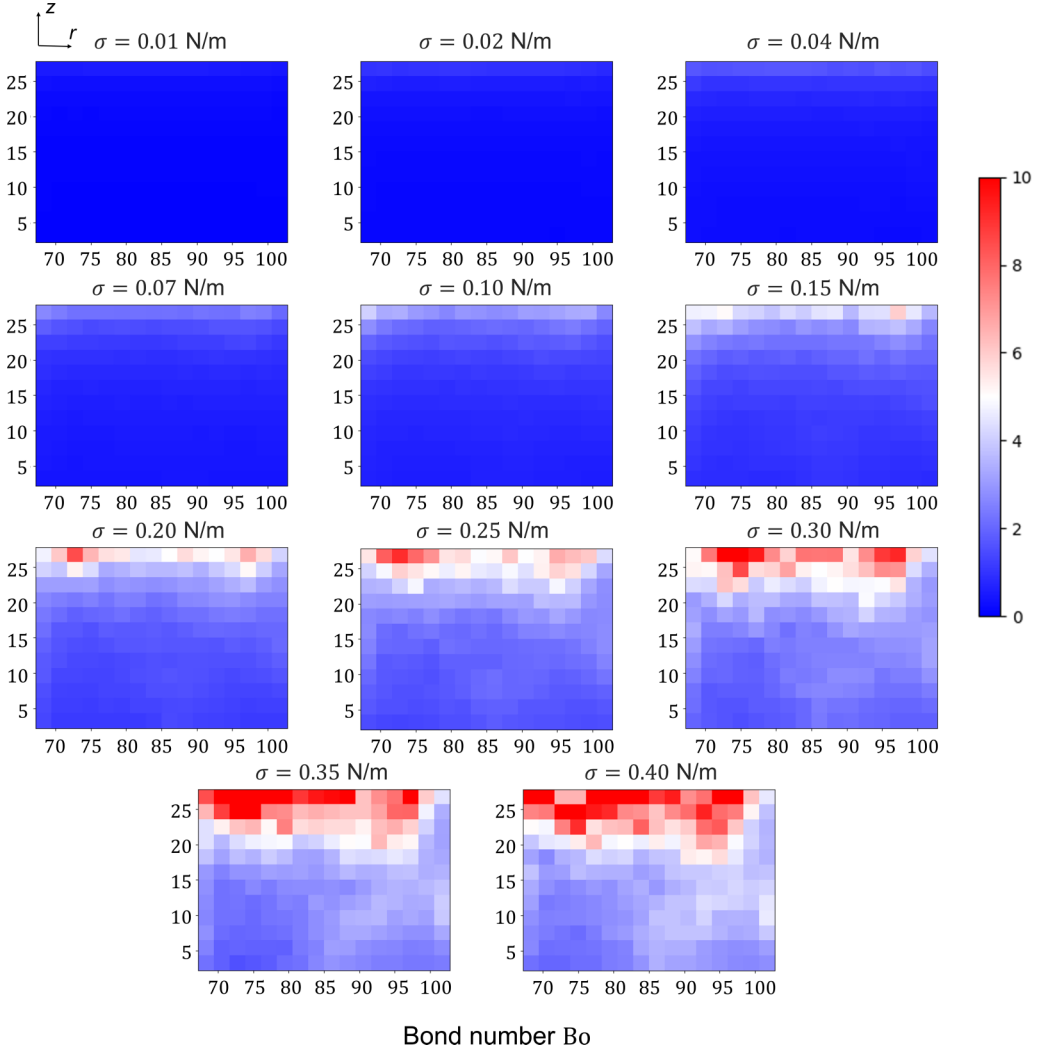


FIG. 11. Coarse-grained Bond number in a cohesive split-bottom cell for different values of surface tension  $\sigma$  and a rotational rate  $\Omega = 0.16$  rad/s. The values of  $Bo$  have been capped at 10 to facilitate the comparisons.

It is important to note that which dimensionless parameter is needed to describe cohesive rheologies is still an open question and that other propositions are possible. For instance, Mandal *et al.* [46] proposed an effective cohesive number involving additional grain interaction properties while Macaulay and Rognon [89] used two numbers to define cohesion, the cohesion-strength and the cohesion-energy. Since the particle's stiffness dependence is not considered here and that only quasistatic flows are investigated, i.e., low-cohesion energy, the Bond number coupled to the critical state assumption (see Sec. VB 1) has been preferred over the other choices.

The Bond number  $Bo$  is plotted in Fig. 11 to conclude this series of qualitative analysis inside the cohesive split-bottom geometry. For ease of comparison, the color scale is limited to values  $Bo \leq 10$ . The maximum bonding force between two particle  $F_{\text{Imax}}^{P-P}$  being constant for a fixed surface tension, the local variations in  $Bo$  are solely originating from the changes in pressure. Hence, the Bond number profiles are simply the inverse transformation of the pressure profiles shown in Appendix C. An important consequence is the nondependency of  $Bo$  on the radius for low

to medium values of  $\sigma$ . Indeed, due to the hydrostatic-like profiles, a unique Bond number (and pressure) is associated to each height  $z$  so that  $\text{Bo} = \text{Bo}(z)$ . This specific feature will be of great importance for more in-depth analysis and will be detailed in the following section.

Additional fields such as shear stress  $\tau$ , pressure  $P$ , strain rate  $\dot{\gamma}$ , and stress ratio  $\mu$  are shown and commented in Appendix C.

All of the aforementioned observations confirm the intuitive idea that cohesive materials do not behave in a similar way to dry ones and that specific models are necessary to accurately simulate them. While some local rheologies have been provided with cohesive extension such as the  $\mu(I)$  rheology [56,90], nonlocal theories, including the NGF rheology, are for the most part limited to dry particles without bonding forces. However, cohesion does not only affect the local behavior but also has an influence on the propagation of nonlocal effects. The apparition of heterogeneities, i.e., flowing and static coexisting regions, is an example. Similar observations have been realized by a recent study of Mandal *et al.* [46] who highlighted the strong relationship between adhesion, shear banding, hysteresis and nonlocal effects within a planar shear cell, and that increasing adhesion increases the tendency toward shear localization. Since the physical assumptions made for the derivation of the  $\mu(I)$ , NGF, or GEM are not equivalent, unexpected differences might show up when applied to more complex systems. To obtain a rigorous description of cohesion influence within nonlocal granular flows, it is crucial to determine a new constitutive relationship between the granular fluidity and the degree of cohesiveness, i.e., between  $g$  and  $\text{Bo}$  in the present work. With this objective in mind, a detailed quantitative analysis of the different tensorial fields is performed in the next section.

## B. Cohesive constitutive law for granular fluidity

### 1. Quantitative analysis

A quantitative analysis is performed with the hope of extracting new physical laws relating the macroscopic fields introduced earlier to one another, and especially their dependency on cohesiveness, i.e., Bond number. Since the final objective of this work is to develop a new constitutive for the NGF model, a particular attention is given to the granular fluidity  $g$ .

To derive new constitutive laws from such dataset and control the spreading, it is necessary to either transform or limit the range of used data so that the macroscopic quantities are well-defined, i.e., only the local data which achieved the critical state are exploited. The critical state is defined as the state where the material deforms with applied strain without any change in the normal stress, shear stress and solid fraction and has its origin in solid mechanics [91]. A common way to define the critical state within the split-bottom cell geometry is to consider the points where the condition  $\gamma \geq 1$  is satisfied [92,93]. This state is therefore independent of the initial conditions and rules out the solid clusters which do not deform. Practically, only the shear band data points where the strain rate is maximum are used for data analysis and condition based on the local strain rate is used [56,75]. According to the study from Roy *et al.* [56], the critical state is achieved for  $\dot{\gamma} > \zeta \dot{\gamma}_{\max}(z)$  where  $\dot{\gamma}_{\max}(z)$  is the maximum strain rate a given height and  $\zeta$  is an empirically derived cut-off threshold.

In the shear band area where the critical state is assumed, the local shear stress  $\tau$  becomes independent of the local strain rate  $\dot{\gamma}$  and  $\tau/P$  becomes constant. Consequently, to each value of  $P$  (and  $z$ ) a unique value of  $\mu$  is associated so that  $\mu$  is well defined and no spread of data points is observed anymore. The plots for both  $\mu$  and  $g$  truncated by the cut-off values  $\zeta = 0.1$  and  $0.8$  (similar to Ref. [56]) are shown in Fig. 12. Each plot is constructed from the entire set of data points from the coarse-graining domain, where one data point corresponds to the averaged field value within a distinct RVE (Fig. 2). The  $\dot{\gamma} > 0.1\dot{\gamma}_{\max}(z)$  plots still present a significant spread for each  $\sigma$ . Contrarily, the  $\dot{\gamma} > 0.8\dot{\gamma}_{\max}(z)$  profiles show an important rupture. The number of data points has been drastically reduced and no vertical overlapping of data is observed within each  $\sigma$  set, i.e., the critical state has been achieved. Particular shapes are now visible, in particular the subplot (D) which reveals two distinct lines, reinforcing the cohesion-extended  $\mu(I, C)$  rheology. The two lines

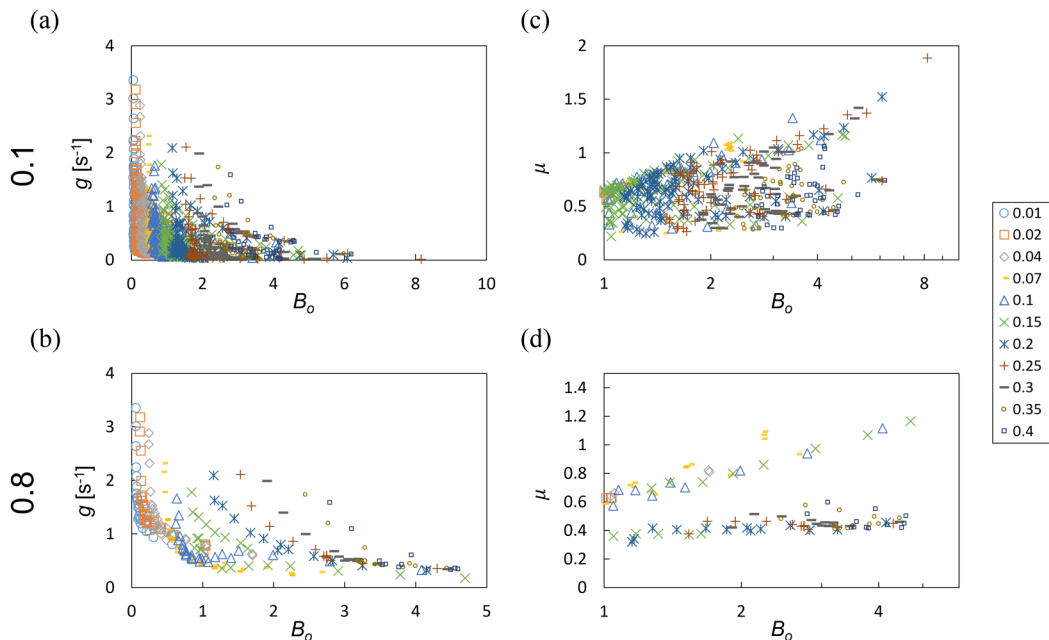


FIG. 12. Granular fluidity (a and b, linear scale) and stress ratio (c and d, logarithmic scale) limited to RVE whose strain rate  $\dot{\gamma}$  is greater than (a and c)  $0.1\dot{\gamma}_{\max}$  and (b and d)  $0.8\dot{\gamma}_{\max}$ .

represent the two shear bands developing within the cell (Fig. 22), the upper lines corresponds to the central-left shear band while the lower one corresponds to the shear band developing near the outer wall for highly cohesive cases. The separation in two separate lines is due to the difference in magnitude and distribution of shear and normal stresses as well as strain rate. The quasiconstant shape of the second branch is due to the solid regime developing within the cell. For  $\sigma \geq 0.15$  N/m, the internal field almost moves as a unique body. The moving particles near the outer wall are not dragging the internal particle anymore and finally two distinct regions just slide over each other. The same behavior is observed for higher values of  $\sigma$ , the shear band delimiting the two sliding region has reached an equilibrium, hence the stagnation of the stress.

Regarding the granular fluidity  $g$ , which is the principal field of interest in this work, no clear profile has been unearthed and the data points are still fairly scattered. The shattered distribution implies that the Bond number is not enough to explain the fluidity and that more variables should be considered in its expression, i.e., it is necessary to find a suitable normalization.

## 2. Normalization of the granular fluidity

Ideally, there exists a normalization that could gather all the data points from the considered fluidity set on a single curve so that every external contributions, at the exception of the influence of cohesion, are removed from the analysis. For instance, a similar approach has been used in the literature for the granular viscosity in a granular bed sheared by a rotating impeller [94]. Although the validity is subject to questions for highly cohesive cases where the shear band definition becomes ambiguous, each normalization and discussion presented in this section are based on the aforementioned critical-state local data which respect the  $\dot{\gamma} > 0.8\dot{\gamma}_{\max}(z)$  condition [Fig. 12(b)]. One may rewrite this condition in terms of shear strain  $\gamma$  by using the averaging time,  $t_{\text{av}} = 5$  s in this work:

$$\gamma \geq 0.8\dot{\gamma}_{\max}(z) \times t_{\text{av}} = \gamma_c. \quad (29)$$

Due to the variations of  $\dot{\gamma}_{\max}(z)$  with the layer height  $z$  and the surface tension  $\sigma$ , no general value of  $\gamma_c$  can be derived. However, by setting the height and the surface tension, e.g.,  $z = 21$  mm and  $\sigma = [0.01, 0.15, 0.30]$ , we obtain representative values of the critical shear strain  $\gamma_c(z = 21 \text{ mm}) = [2.04, 1.36, 0.96]$ , respectively. The strain threshold is maximum for lowly cohesive cases, and tend to decrease for high surface tension values which limit the fluidization of the particles. Estimates of critical shear strain values  $\gamma_c$  for different combinations of height and surface tension can be obtained in a similar fashion by applying Eq. (29).

Now the important question is “What normalization of the granular fluidity should be chosen?” Unfortunately, due to the ongoing concerns and investigations regarding the fluidity phenomenology there is no clear-cut answer as to which parameters should be used for its normalization. Nonetheless, a consensus exists regarding the strong relationship between the granular fluidity (and more generally nonlocalities) and both velocity fluctuations  $V'$  and particles diameter  $d$ , as shown in the work of Zhang and Kamrin [43]. Therefore, it has been decided to use the macroscopic quantity  $T$ , usually referred to as granular temperature to describe the fluidity. This field is at the foundation of the nonlocal kinetic theory and represents the squared average of velocity fluctuations. Moreover, its relationship with the granular fluidity has been a recent topic of interest [43,61] and encourages its use in such operation. The granular temperature is defined by the following equation:

$$T = \frac{1}{3N} \sum_{i \in V_{\text{rve}}} \sum_{j=1,2,3} (V'_{ij})^2, \quad (30)$$

where  $V'_{ij} = V_{ij} - \langle V_{ij} \rangle$  is the  $j$  component of the velocity fluctuation of particle  $i$  and  $\langle V_{ij} \rangle$  the spatially averaged particle velocity over a RVE,  $N$  is the number of particles. To guarantee the physical meaning of the results, it is crucial that values of  $\langle V_{ij} \rangle$  are calculated for each time step, i.e., the temporally averaged values of  $\langle V_{ij} \rangle$  should not be used for the calculation of  $V'_{ij}$ . Once the granular temperature has been computed for each time step, the temporal average is realized over each snapshot.

Similar to the plots from Sec. V A, a preview of the granular temperature evolution for different values of surface tension  $\sigma$  is displayed in Fig. 13. As expected, the velocity fluctuations are localized in the same areas as granular fluidity (Fig. 10) or strain rate (Appendix C), i.e., within the shear band. At first, the magnitude steadily decreases due to the vanishing of the central shear band. It then grows back and accompanies the formation of the second shear band near the outer wall.

Using this newly calculated  $T$  field, a first expression of the normalized fluidity  $\bar{g}$  can be derived:

$$\bar{g} = \frac{gd}{\sqrt{T}}. \quad (31)$$

The normalized fluidity is again plotted with respect to the Bond number in Fig. 14. Compared to the raw data from Fig. 12(b), the normalized data are much less scattered and start collapsing onto a master curve. Two propositions are given for a fitted model, an exponential curve for subplot (solid line) and a third degree polynomial curve in subplot (dashed line).

The two master curves are, respectively, expressed as

$$\bar{g} = \frac{gd}{\sqrt{T}} = 1.219 \exp(-0.527\text{Bo}), \quad (32)$$

$$\bar{g} = \frac{gd}{\sqrt{T}} = 1.2417 - 0.6321\text{Bo} + 0.1245\text{Bo}^2 - 0.0084\text{Bo}^3. \quad (33)$$

Both curves give similar performances with high correlation coefficients  $R^2 = 0.968$  and  $0.969$ , respectively. Equations (32) and (33) are the first tentative constitutive equations for a cohesive nonlocal framework based on the NGF rheology. For simplicity, only exponential fitting curves will be considered henceforth.



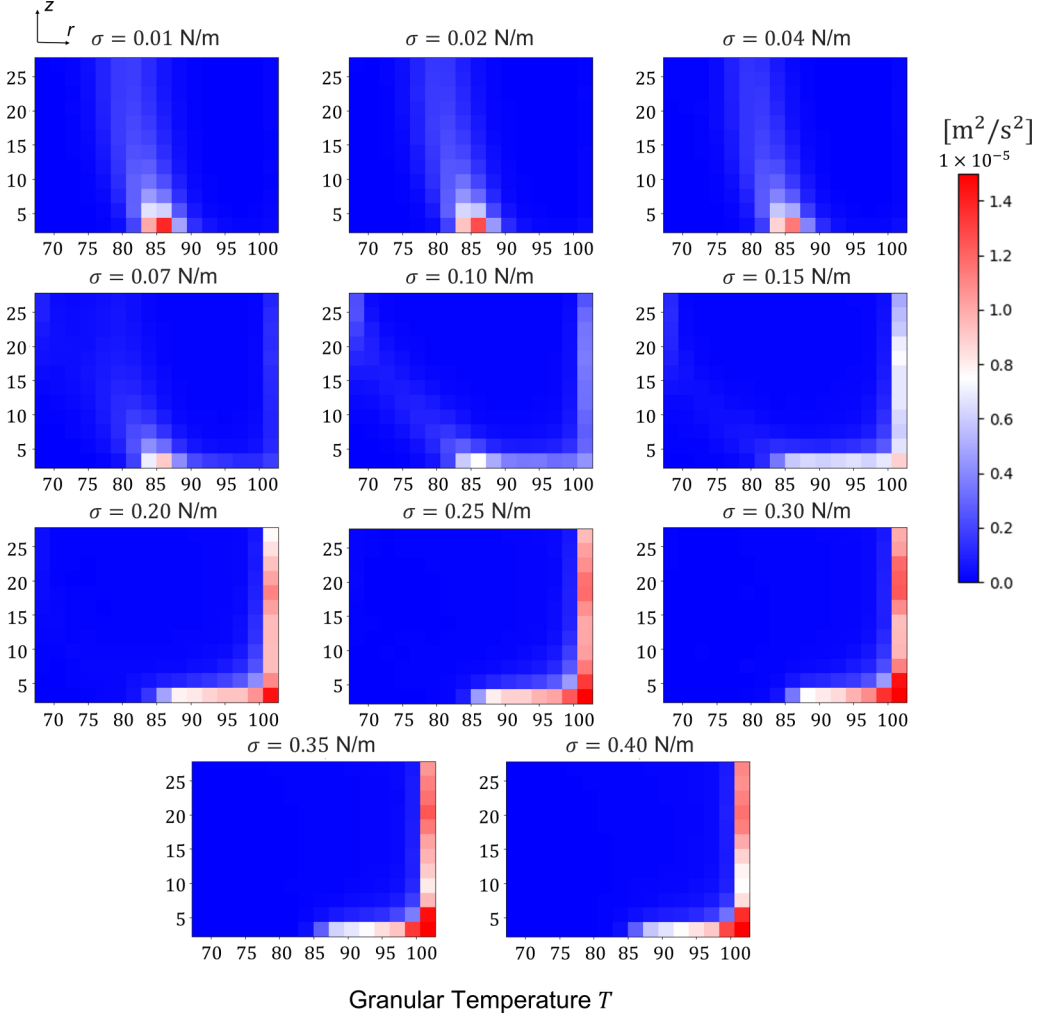


FIG. 13. Coarse-grained granular temperature in a cohesive split-bottom cell for different values of surface tension  $\sigma$  and a rotational rate  $\Omega = 0.16$  rad/s.

Other normalizations of granular fluidity are available in the literature and could potentially have a significant effect on the constitutive model accuracy due to the contribution of additional parameters. Indeed, besides the velocity fluctuations and particles diameter, it has been found that the volume fraction  $\phi$  also plays an important role in the granular fluidity description. Following the work of Zhang and Kamrin [43], the fluidity of dry granular materials is expressed using a hyperbola  $F(\phi)$ :

$$F(\phi) = \frac{-(\phi - 0.58) + \sqrt{(\phi - 0.58)^2 + 1.54 \times 10^{-4}}}{0.048} + 2, \quad (34)$$

so that the normalized fluidity becomes

$$\bar{g} = \frac{gd}{\sqrt{T}F(\phi)}. \quad (35)$$

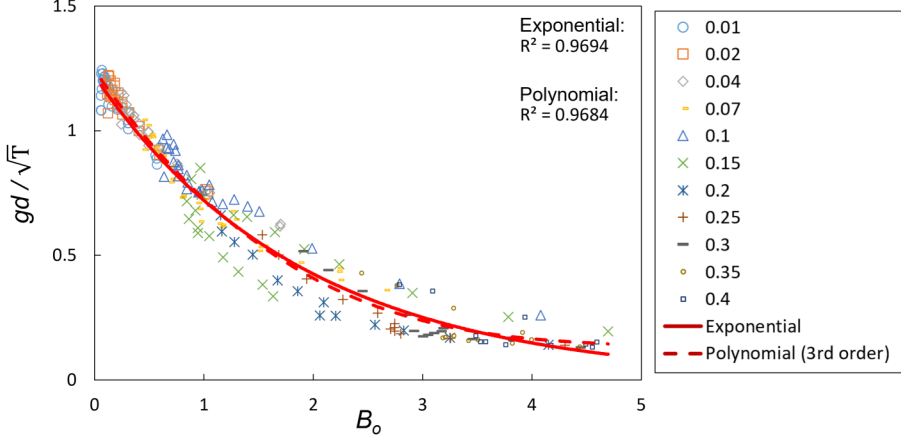


FIG. 14. Granular fluidity normalized with respect to the average particle diameter  $d$  and granular temperature  $T$  for the points satisfying the  $\dot{\gamma} > 0.8\dot{\gamma}_{\max}(z)$  condition. The data sets are completed with fitted curves: exponential (solid line) and third-order polynomial (dashed line).

However, this empirically based derivation of  $F(\phi)$  is only one of the various ways to relate the fluidity to the granular temperature. To explore other promising normalizations, the Kinetic theory which relates the states variables of the system to the granular temperature is considered. Based on the work of Lun *et al.* [95], the pressure  $P$  and viscosity  $\eta$  of the granular material can be expressed as functions of  $T$  and  $\phi$ ,

$$P = \rho[1 + 2(1 + e)\phi f_0(\phi)]T, \quad (36)$$

$$\eta = \frac{8}{3\sqrt{\pi}}d\rho\phi f_0(\phi)\sqrt{T}, \quad (37)$$

where  $f_0$  is the Carnahan-Starling expression for the radial distribution function at contact [96]:

$$f_0(\phi) = \frac{1}{1 - \phi} + \frac{3\phi}{2(1 - \phi)^2} + \frac{\phi^2}{2(1 - \phi)^3}. \quad (38)$$

Eqs. (36) and (37) can be written in shortened forms:

$$P(\phi, T) = \rho F_1(\phi)T, \quad (39)$$

$$\eta(\phi, T) = \rho d F_2(\phi)\sqrt{T}, \quad (40)$$

with  $F_1(\phi) = 1 + 2(1 + e)\phi f_0(\phi)$  and  $F_2(\phi) = 8/(3\sqrt{\pi})\phi f_0(\phi)$ . The operational definition of the fluidity then implies

$$g = \frac{\dot{\gamma}}{\mu} = \frac{P}{\eta} = \frac{\rho F_1(\phi)T}{\rho d F_2(\phi)\sqrt{T}} = \frac{\sqrt{T}}{d} \frac{F_1(\phi)}{F_2(\phi)}. \quad (41)$$

Defining  $F_k(\phi) = F_1(\phi)/F_2(\phi)$ , the normalized fluidity writes

$$\bar{g} = \frac{gd}{\sqrt{T}F_k(\phi)}. \quad (42)$$

Finally, a last normalization which relates the granular fluidity to the inertial number  $I$  and the dimensionless granular temperature  $\Theta$  is explored [61]. The normalized granular fluidity is

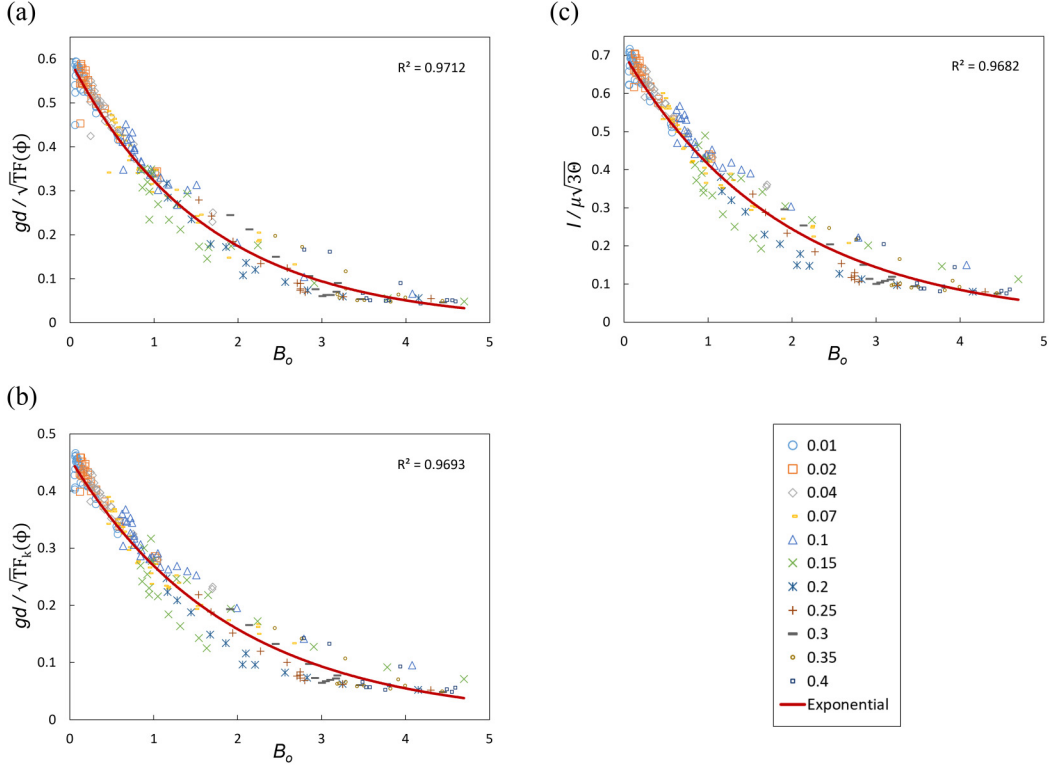


FIG. 15. Normalized granular fluidity plotted with respect to the Bond number for various surface tensions  $\sigma$  and fitted with exponential curves. (a) Eq. (35), (b) Eq. (42), and (c) Eq. (43). Only the points satisfying the  $\dot{\gamma} > 0.8\dot{\gamma}_{\max}(z)$  condition are plotted.

expressed by the following relation:

$$\bar{g} = \frac{I}{\mu\sqrt{3\Theta}}, \quad (43)$$

with  $\Theta = \rho_s T/P$ . The definition of the inertial number is recalled:

$$I = \frac{\dot{\gamma}d}{\sqrt{P/\rho_s}}. \quad (44)$$

All three normalized datasets given by Eqs. (35), (42), and (43) are shown in Figs. 15(a), 15(b), and 15(c), respectively. For each figure, an exponential fitted curve is given:

$$\bar{g} = \frac{gd}{\sqrt{TF}(\phi)} = 0.596 \exp(-0.614Bo), \quad (45)$$

$$\bar{g} = \frac{gd}{\sqrt{TF_k}(\phi)} = 0.457 \exp(-0.53Bo), \quad (46)$$

$$\bar{g} = \frac{I}{\mu\sqrt{3\Theta}} = 0.703 \exp(-0.528Bo). \quad (47)$$

Each normalization gives similar results, equation parameters, and correlation coefficients ( $R^2 \approx 0.97$ ). No significant improvements have been observed compared to the first normalization shown in Fig. 14, the influence of the volume fraction variations does not seem indispensable to obtain

physical predictions of cohesive flows. The spread of each subplot, although slightly different from one another, remains comparable and does not give solid ground as to which definition of granular fluidity is the most physically accurate or appropriate. On the contrary, these results tend to indicate that these three definitions of the granular fluidity are equivalent and interchangeable.

Finally, the spread of data points in every normalization could also come from the choice of dimensionless number, i.e., the Bond number. The Bond number is one of the simplest of quantifying cohesion influence and only relates the maximum liquid bridge force to the confining pressure. However, additional contributions might be necessary to fully grasp the cohesion influence on the flow field, e.g., the cohesion-energy [89] which also considers the kinetic energy of the particles. However, there is no clear answer as to how to model cohesion in granular flows and there is no guarantee that using the cohesion-energy in addition to the Bond number could improve the current trendlines, especially for quasistatic flows as presented in this work.

## VI. CONCLUSION

Cohesion in split-bottom flows have been successfully observed and major deviations from the dry behavior have been visualized thanks to the coarse-graining procedure, calling for updated rheologies. For instance, the arrangement of quasistatic areas into large clusters which act like solids, i.e., resist high shearing and emphasize the volume fraction disparities, is an important divergence from dry rheologies. The shear band characterized by the velocity, strain rate, fluidity, velocity fluctuations and volume fraction, has also been observed to be extremely dependent on cohesion and has shown varying locations, widths and magnitudes. The transformation of the quasihydrostatic profile of the pressure field toward a more patchy distribution has also been observed and related to similar changes in Bond number values. Overall, cohesion has been observed to enhance heterogeneities, shear localization, and nonlocalities within granular flows.

Facing the necessity for updated cohesive constitutive laws, extensive analyses have been performed to uncover a relation between the granular fluidity from the NGF model and the Bond number. After limiting the scope to critical state quantities, a clear dependence of the fluidity on the Bond number has been highlighted. Highly cohesive bonds prevent the particles to move, limiting the velocity fluctuations within the domain and the plastic events from occurring, i.e., weaker granular fluidity. Several normalizations based on the granular temperature from the kinetic theory have been proposed to isolate the contribution of cohesion on the granular fluidity. Following the microscopic phenomenology of the granular fluidity whose main contributions are the particles size and the velocity fluctuations, a first normalization solely based on the granular temperature and the particles diameter was applied. This first normalization had the effect of reducing the spread of the data points onto a master curve following an exponential-type decay (or third order polynomial), giving a first tentative law for cohesive material. Additional normalizations have been explored to account for the volume fraction and precise the physical definition of the granular fluidity. However, no visible influence has been observed and similar exponential laws have been derived. These results suggest that the volume fraction fluctuations are not essential for the construction of a continuous, cohesive fluidity field and that liquid bridges influence predominates.

Furthermore, the promising results made by using the granular temperature field consolidate the recent studies regarding a relationship between the NGF rheology and the kinetic theory [43,61]. However, to implement these new constitutive laws and evaluate their performance, it is now necessary to derive one more law for the granular temperature so that the system can be closed. Further efforts should be made in this direction to explore the interrelation between NGF and the kinetic theory so that a unified framework could possibly take shape, as well as to complete the first cohesive-extended, nonlocal continuum model. The remaining slight spread of data suggests that the derived constitutive laws could be enhanced even further by either including more variables within the normalization or changing the way cohesion is quantified, i.e., changing the definition of the Bond number.

The fact that the data used for the construction of the cohesive laws have been limited to the critical state, i.e., within the shear band, may lead to interrogations regarding the universality of the proposed model. Indeed, the influence of the creeping, almost static, areas has not been considered. The model could possibly fall short in these specific regions. It is however unlikely that the critical state limitation imposed in this work leads to major discrepancies in the creeping areas. Due to the velocity magnitude being several orders of magnitude lower in creeping regions than in the rest of the domain, the resulting error would be of similar order and therefore, be beyond the current accuracy of the NGF rheology. Nevertheless, only the practical implementation of the proposed cohesive NGF equations will make it possible to quantify such error, and either confirm or invalidate the tentative laws exposed in this work.

Finally, the possibility of improving the current data collapses by completing the Bond number with another dimensionless number such as the cohesion-energy is not excluded and is kept for future work.

#### ACKNOWLEDGMENTS

A part of the study was supported by JSPS KAKENHI Grant No. JP22K03926. All of the computations were carried out using the computer resource in Research Institute for Information Technology, Kyushu University.

#### APPENDIX A: CONTACT MODEL

Unlike the aforementioned continuum NGF model, each particle within the granular bed is tracked individually in DEM. Every single particle has its own set of variables such as mass  $m_i$ , diameter  $d_i$ , velocity  $\mathbf{V}_i$ , angular velocity  $\boldsymbol{\omega}_i$ , position  $\mathbf{x}_i$ , etc. that controls its behavior at each time step and give rise to mechanical forces during contacts between two particles.

In this paper, the interparticle interactions are modelled using the soft-sphere model [62]. In this model, the particles are considered geometrically rigid with the exception of the finite contact duration in which the particles are assumed to be deformable. The deformation of two particles colliding is represented by an overlap  $\delta_n$  as shown in Fig. 16. The soft-sphere model can account for more than two particles colliding with one another at the same time and is consequently applicable to the study of dense systems where particles have constant frictional contacts with neighbors.

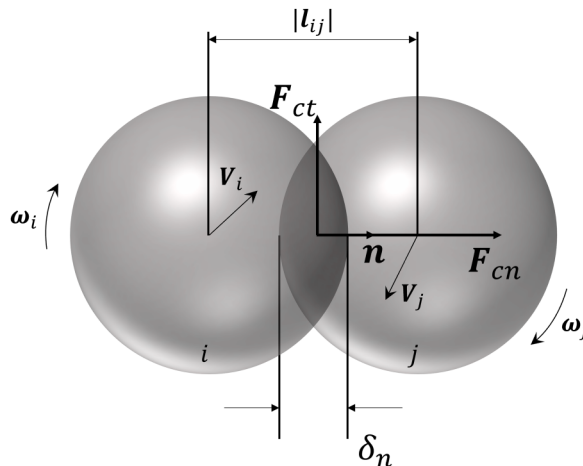


FIG. 16. Contact between two particles in the soft-sphere model.

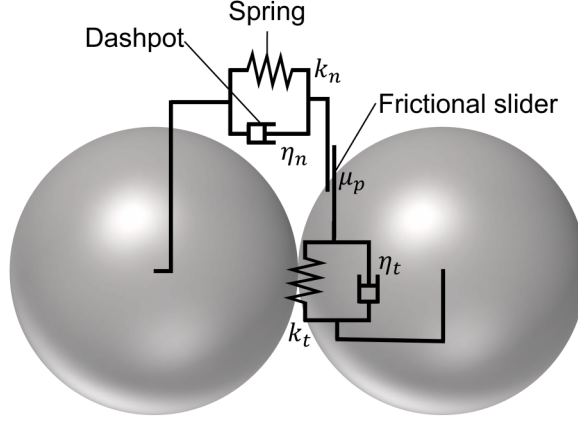


FIG. 17. Contact force in the soft-sphere model.

Once a pair  $(i, j)$  of particles contacts, the normal and tangential contact forces  $\mathbf{F}_{cnij}$  and  $\mathbf{F}_{ctij}$  are calculated with respect to the magnitude and rate of the overlap. All the forces applied to a same particle are summed to get the force balance acting on it. The motion of the particle, i.e., acceleration, velocity and position, can then be determined from this force. The procedure is repeated for every particle in the simulation until the entire set of positions is achieved. Finally, the same sequence is looped over a definite number of time steps to complete the DEM simulation.

The particles motion is based on Newton's second law:

$$m_i \dot{\mathbf{V}}_i = \sum_j (\mathbf{F}_{cij} + \mathbf{F}_{lij}) + \mathbf{F}_{Gi}, \quad (\text{A1})$$

$$I_i \dot{\boldsymbol{\omega}}_i = \sum_j (\mathbf{T}_{cij} + \mathbf{T}_{lij}), \quad (\text{A2})$$

where  $\dot{\mathbf{V}}_i$  is the particle acceleration,  $\mathbf{F}_{cij} = \mathbf{F}_{cnij} + \mathbf{F}_{ctij}$  is the contact force applied by particle  $j$  on particle  $i$ ,  $\mathbf{F}_{lij}$  is the force exerted by the liquid bridge from particle  $j$  on particle  $i$ ,  $\mathbf{F}_{Gi} = m_i \mathbf{G}$  is the gravitational force with  $\mathbf{G}$  the gravitational acceleration,  $I_i$  is the particle moment of inertia,  $\dot{\boldsymbol{\omega}}_i$  is the angular acceleration,  $\mathbf{T}_{cij}$  is the contact torque between the particles  $(i, j)$  and  $\mathbf{T}_{lij}$  is the torque exerted on the particle  $i$  due to the liquid bridge with particle  $j$ . In the soft-sphere model, the normal and tangential contact forces are usually represented by a combination of springs, dashpots and frictional sliders as illustrated in Fig. 17, with  $k_n$ ,  $\eta_n$ ,  $k_t$ ,  $\eta_t$  the spring stiffness and the dashpot damping coefficient in the normal and tangential directions and  $\mu_p$  the sliding friction coefficient. The horizontal spring and dashpot represent, respectively, the elastic repulsion force and the energy dissipation in the normal direction, i.e., from one particle center to that of the other. However, the vertical elements represent the tangential component of the contact force with the static friction (spring-dashpot) and the dynamic force (frictional slider). In this work, cohesive viscous forces are ignored [52,53] so that the cohesive interactions between two particles are solely described through capillary forces. The capillary forces have for orientation the straight line passing through the centers of the two particles and are purely normal so that they do not induce torque. Eq. (A2) can then be simplified as

$$I_i \dot{\boldsymbol{\omega}}_i = \sum_j \mathbf{T}_{cij}. \quad (\text{A3})$$

The Hertzian model [63] is applied so that the contact force in the normal direction between two particles has two terms, a spring force and a damping force:

$$\mathbf{F}_{cnij} = -k_n \delta_n^{3/2} \mathbf{e}_{nij} - \eta_n \mathbf{V}_{nij}, \quad (\text{A4})$$

where  $k_n$  is the normal stiffness of the spring,  $\delta_n$  is the normal overlap between the two particles,  $\eta_n$  is the normal damping coefficient of the dashpot,  $\mathbf{V}_{nij}$  is the normal relative velocity of particle  $i$  to particle  $j$  and  $\mathbf{e}_{nij}$  is the unit vector from the center of particle  $i$  to particle  $j$ .

The tangential component of  $\mathbf{F}_{cij}$ , based on the Mindlin model [64], also presents two terms, a static friction and a shear force (frictional slider and spring-dashpot in Fig. 17):

$$\mathbf{F}_{ctij} = \min [-k_t \delta_t \mathbf{e}_{tij} - \eta_t \mathbf{V}_{tij}, \mu_p |\mathbf{F}_{cnij}| \mathbf{e}_{tij}], \quad (\text{A5})$$

with  $k_t$  the tangential stiffness,  $\delta_t$  the tangential overlap,  $\eta_t$  the tangential damping coefficient, and  $\mu_p$  the friction coefficient between two particles. The tangential relative velocity at the contact surface between two particles ( $i, j$ ) is derived from both translational  $\mathbf{V}_n$  and angular velocities  $\boldsymbol{\omega}$ :

$$\mathbf{V}_{tij} = \mathbf{V}_{ij} - \mathbf{V}_{nij} + [(d_i/2)\boldsymbol{\omega}_i + (d_j/2)\boldsymbol{\omega}_j], \quad (\text{A6})$$

with  $\mathbf{V}_{ij} = \mathbf{V}_i - \mathbf{V}_j$  the relative velocity between particles and  $d$  the particle diameter. The unit tangent vector  $\mathbf{e}_{tij}$  is based on the tangential relative velocity direction

$$\mathbf{e}_{tij} = \frac{\mathbf{V}_{tij}}{|\mathbf{V}_{tij}|}. \quad (\text{A7})$$

The term  $\mu_p |\mathbf{F}_{cnij}| \mathbf{e}_{tij}$  in Eq. (A5) corresponds to the Coulomb friction and acts as a limiting value for the tangential force. It is important to not mistake the friction coefficient  $\mu_p$  with the stress ratio  $\mu$  (or  $\mu_s$ ) introduced in the continuum approach,  $\mu_p$  is a microscopic quantity characterizing the friction between two particles while  $\mu$  is an effective macroscopic field based on averaged scales. The resulting contact force and torque between two dry particles (without rolling friction) is then given by

$$\mathbf{F}_{cij} = \mathbf{F}_{cnij} + \mathbf{F}_{ctij}, \quad (\text{A8})$$

$$\mathbf{T}_{cij} = (d_i/2)\mathbf{e}_{nij} \times \mathbf{F}_{ctij}, \quad (\text{A9})$$

where the stiffness constants are given by

$$k_n = \frac{\sqrt{d}E}{3(1-\Gamma^2)} \quad \text{and} \quad k_t = \frac{2\sqrt{d}S}{2-\Gamma} \delta_n^{1/2}, \quad (\text{A10})$$

with  $E$  the Young's modulus,  $\Gamma$  the Poisson's coefficient of the particle material and  $S = E/2(1 - \Gamma)$  the shear modulus. The expressions of the damping coefficients,  $\eta_n$  for the normal direction and  $\eta_t$  for the tangential direction are based on the work of Tsuji *et al.* [97] who proposed a relation between the normal damping coefficient and the well-known coefficient of restitution of particles:

$$\eta_n = a(m_i k_n)^{1/2} \delta_n^{1/4}, \quad (\text{A11})$$

with  $a$  an empirical constant related to the coefficient of restitution. The damping coefficient in the tangential direction  $\eta_t$  is assumed to be equal to  $\eta_n$  in this study.

## APPENDIX B: DETERMINATION OF OPTIMAL PARAMETERS FOR DEM ROUGH WALLS

A three-dimensional Couette cell of dimensions  $R_i = 51$  mm,  $R_o = 63$  mm, and  $H = 10$  mm is illustrated in Fig. 18. The rotational rate of the inner cylinder is fixed at  $\Omega = 0.16$  rad/s. The cell is filled with cohesionless beads of average diameter  $d = 0.75$  mm. The simulation is then run for 15 s. All the DEM parameters are summarized in Table II.

The same coarse-graining method as the one presented in Sec. III B is applied on the geometry to extract the tensorial quantities from microscopic DEM results. Both  $\Delta r$  and  $\Delta z$  are set to 1 mm. Regarding the temporal averaging, only the later times  $10 < t < 15$  are used with a time step of  $\Delta t = 0.1$  s, i.e., 50 snapshots. Finally, the domain in which the coarse-graining procedure is applied

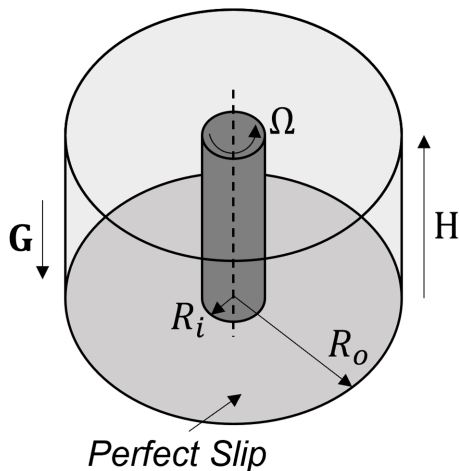


FIG. 18. Three-dimensional Couette cell.

is limited to

$$\begin{aligned} r_{\min} &= 52 \text{ mm} & \text{and} & & r_{\max} &= 62 \text{ mm}, \\ z_{\min} &= 1 \text{ mm} & \text{and} & & z_{\max} &= 9 \text{ mm}, \end{aligned} \quad (\text{B1})$$

written in terms of particle diameter:

$$\begin{aligned} r_{\min}/d &= 69.3 & \text{and} & & r_{\max}/d &= 82.7, \\ z_{\min}/d &= 1.3 & \text{and} & & z_{\max}/d &= 12. \end{aligned} \quad (\text{B2})$$

The velocity magnitude  $|\mathbf{V}|$  at the surface is normalized by the wall velocity  $V_{\text{wall}} = R_i \Omega$  and plotted in Fig. 19(a) for different values of  $R_f$ . The results are compared with profiles obtained using a FVM-based continuum implementation of the steady-state NGF rheology (FVM-NGF) [98,99], whose main parameters have been set to: nonlocal amplitude  $A = 0.48$ , local material parameters  $\mu_s = 0.38$ ,  $\mu_2 = 0.64$ ,  $I_0 = 0.279$ , and density  $\rho_s = 2450 \text{ kg/m}^3$ , which correspond to the values of glass beads. Due to the limited domain of application of the coarse-graining procedure, the velocity near the walls is not measured. From these results, it appears that the coarse-grained velocity is closer from the idealized continuum results for a roughness factor  $R_f \in [0.5, 0.8]$  and starts deviating when the roughness factor either decreases ( $R_f = 0.3$ ) or increases ( $R_f = 1.2$ ). The

TABLE II. DEM parameters for the simulation of the three-dimensional Couette cell.

Properties	Values
Number of particles	439 000
Particle diameter $d$ [mm]	0.75
Initial solid fraction $\phi_0$	0.62
Particle density $\rho_s$ [ $\text{kg/m}^3$ ]	2450
Young's modulus $E$ [Pa]	$5 \times 10^6$
Poisson's Ratio $\Gamma$	0.245
Coefficient of restitution $e$	0.926
Coefficient of friction $\mu_p$	0.16
Gravity magnitude $G$ [ $\text{m/s}^2$ ]	9.81



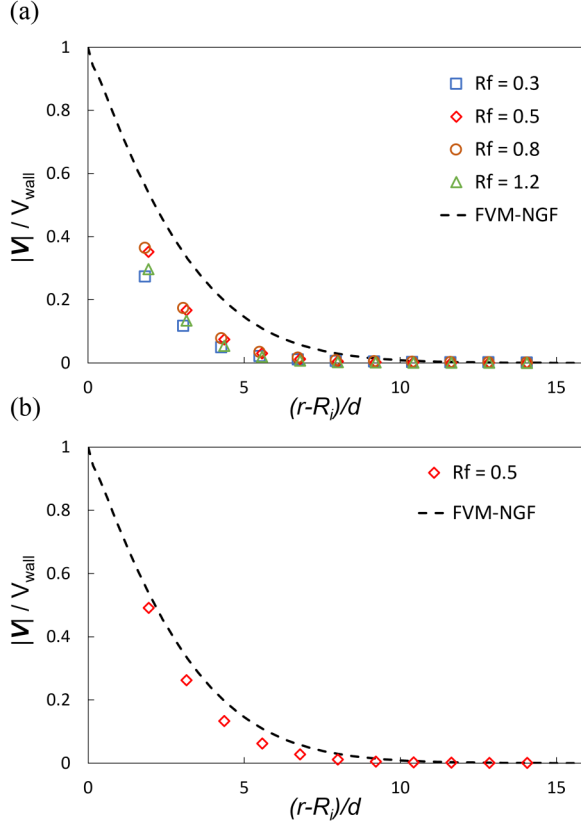


FIG. 19. Couette cell surface velocity profiles for different values of the roughness factor  $R_f$ . (a)  $D_{pl} = 0.1$  mm, (b)  $D_{pl} = 0.3$  mm.

wall-particles must be spaced of roughly half a particle to efficiently drag the internal particles. Consequently, a roughness factor of  $R_f = 0.5$  is chosen in this work.

However, for  $R_f = 0.5$  a noticeable difference between the continuum approach which has a perfect no-slip boundary condition and the DEM results remains. This difference is induced by the presence of the safety plane  $P_l$  located at a distance  $D_{pl} = 0.1$  mm from the wall-particle centers (Fig. 6). This plane is too close from the internal field and interacts with the inner region, smoothing out the velocity field. In the subplot (B), a simulation with  $R_f = 0.5$  is run but this time, the distance  $D_{pl}$  is set to 0.3 mm so that the wall is located further from the centers of the wall-particles. A clear amelioration of the velocity profile is observed. The coarse-grained field is now much closer from the ideal curve and has a behavior corresponding to a no-slip boundary condition. It is essential to place the solid walls as far as possible from the wall-particles to reduce its intrusiveness and have boundaries dominated by particle-particle interactions, it should however satisfies the  $D_{pl} \leq d/2$  condition to avoid that particles from the inner field get stuck between the safety plane and the wall-particles.

A similar verification is realized in the case of the dry split-bottom cell. The geometry, DEM and coarse-graining parameters are identical to the ones used in Sec. IV, at the exception of the surface tension  $\sigma$  which is kept at 0 N/m and the Young Modulus which is set to  $E = 5 \times 10^6$  Pa. We keep the roughness factor at  $R_f = 0.5$  and we set the distance  $D_{pl}$  to 0.559 mm. As shown in Fig. 20, the coarse-grained variables give a good agreement with the results from FVM-NGF [98,99]. Hence, similar values of  $R_f$  and  $D_{pl}$  are kept for the study of cohesive flows within the split-bottom geometry.

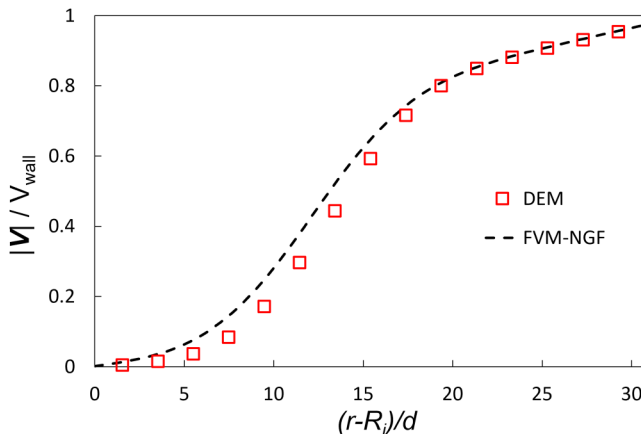


FIG. 20. Coarse-grained surface velocity profile in a dry split-bottom cell.

### APPENDIX C: SNAPSHOTS OF ADDITIONAL COARSE-GRAINED FLOW FIELDS

The normalized velocity  $V_n = |V|/r\Omega$  is shown in Fig. 21 and display a similar behavior as the velocity magnitude presented in Fig. 8. We observe the shift of the shear band toward the inner wall and the split of the shear band near  $\sigma = 0.15$  N/m.

The strain rate field shown in Fig. 22 highlights the splitting of the shear band. At first the strain rate is concentrated in the center area, similar to the dry case, then slowly shifts toward the inner wall. From  $\sigma = 0.10$  N/m and despite the general decrease in magnitude, an additional active area is observed near the outer wall. The overall domain remains motionless while the moving walls fail to shear the internal domain.

Regarding the pressure field presented in Fig. 23, the granular material adopts a quasihydrostatic profile for weak surface tensions, comparable to the dry configuration. However, these standard profiles are slowly disturbed toward more chaotic distributions due to the formation of solid clusters. Eventually, three main regions can be identified: a low pressure region at the top of domain as a direct consequence of the shallow layers, an intermediate region near the shear band on the right which corresponds to the fluidized domain, and finally a high pressure region in the bottom left corner as the outcome of deep, static, solidlike layers.

The shear stress  $|\tau|$  (Fig. 24) has a more peculiar shape and requires a bit more explanations. At first, the shear stress is almost uniformly spread through the entire domain starting from the interface between the static and moving walls  $R_s = 85$  mm. In these low surface tension cases, the granular material, despite the low velocity regime, reacts more like a fluid with a low yield stress. Therefore, the shear stress remains relatively low and does not present strong heterogeneities. However, for higher  $\sigma$ , the material adopts the properties of a solid and in particular its important yield stress. As a result, the magnitude of the shear stress stored in the static domain becomes substantial while the fluidized areas near the walls remain controlled, leading to this bow-shaped pattern.

The aftermath of the last two observations is shown in Fig. 25 which depicts the stress ratio  $\mu = |\tau|/P$ . As explained earlier, the solidification of the material leads to higher shear stress values which in return leads to a general increase of the stress ratio, especially in the top layers where the pressure is low.

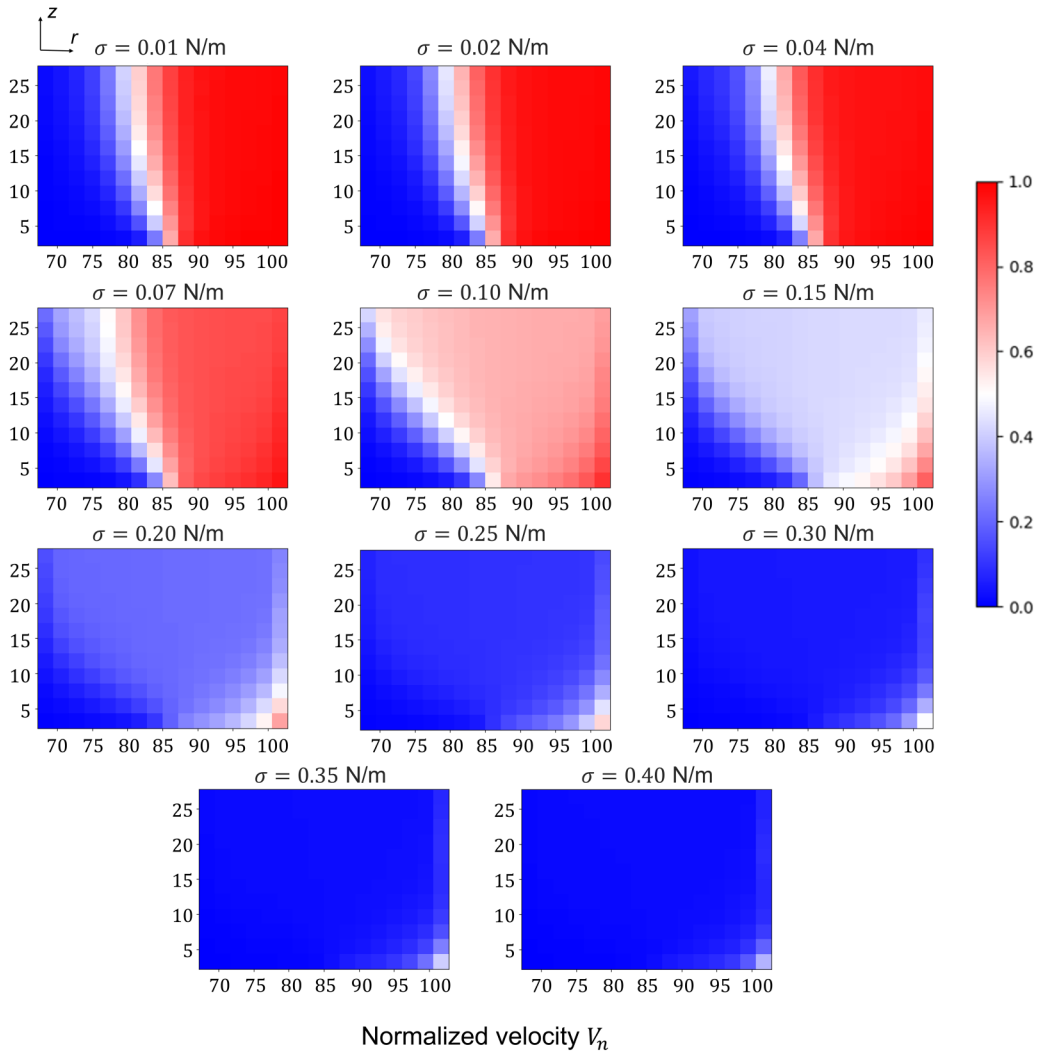


FIG. 21. Coarse-grained normalized velocity in a cohesive split-bottom cell for different values of surface tension  $\sigma$  and a rotational rate  $\Omega = 0.16$  rad/s.

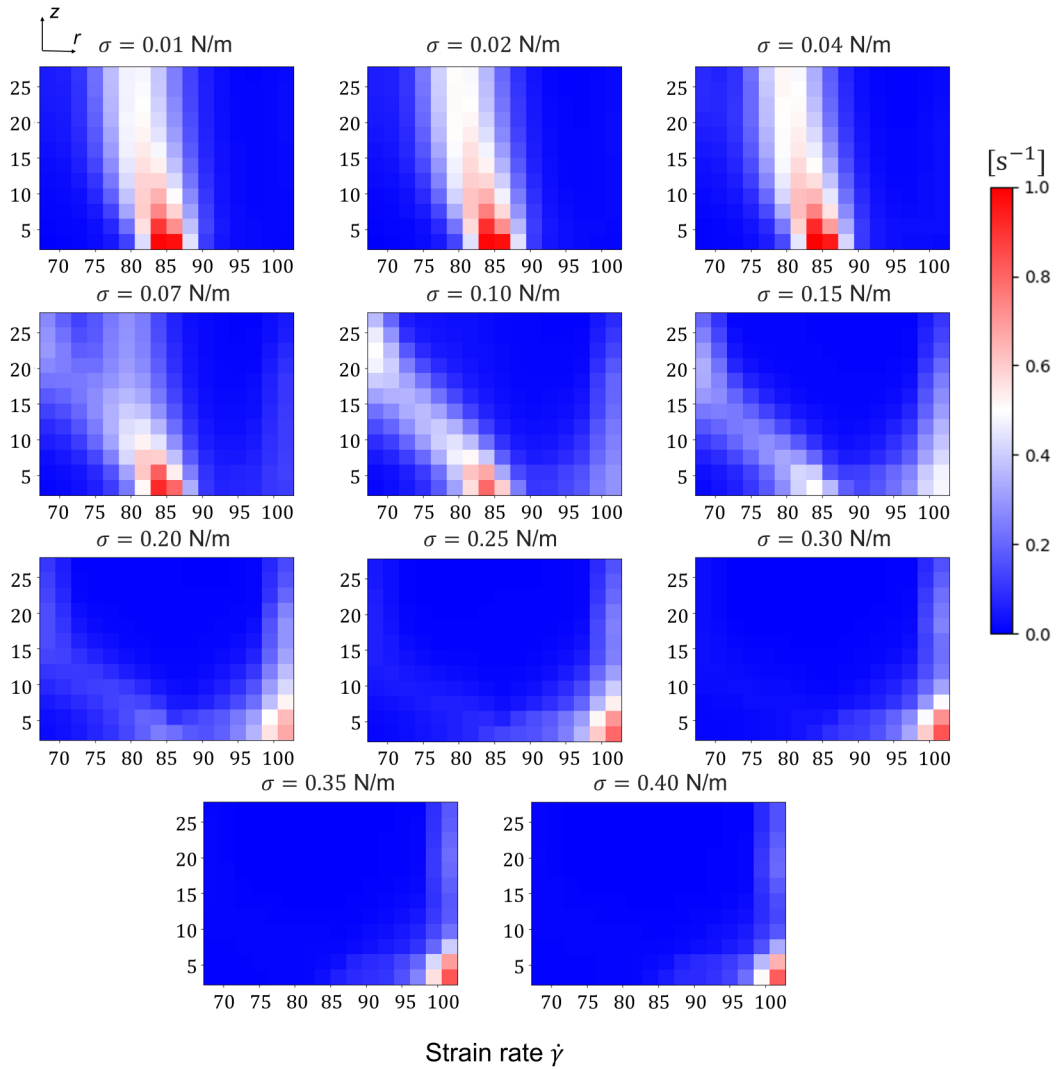


FIG. 22. Coarse-grained strain rate in a cohesive split-bottom cell for different values of surface tension  $\sigma$  and a rotational rate  $\Omega = 0.16$  rad/s.

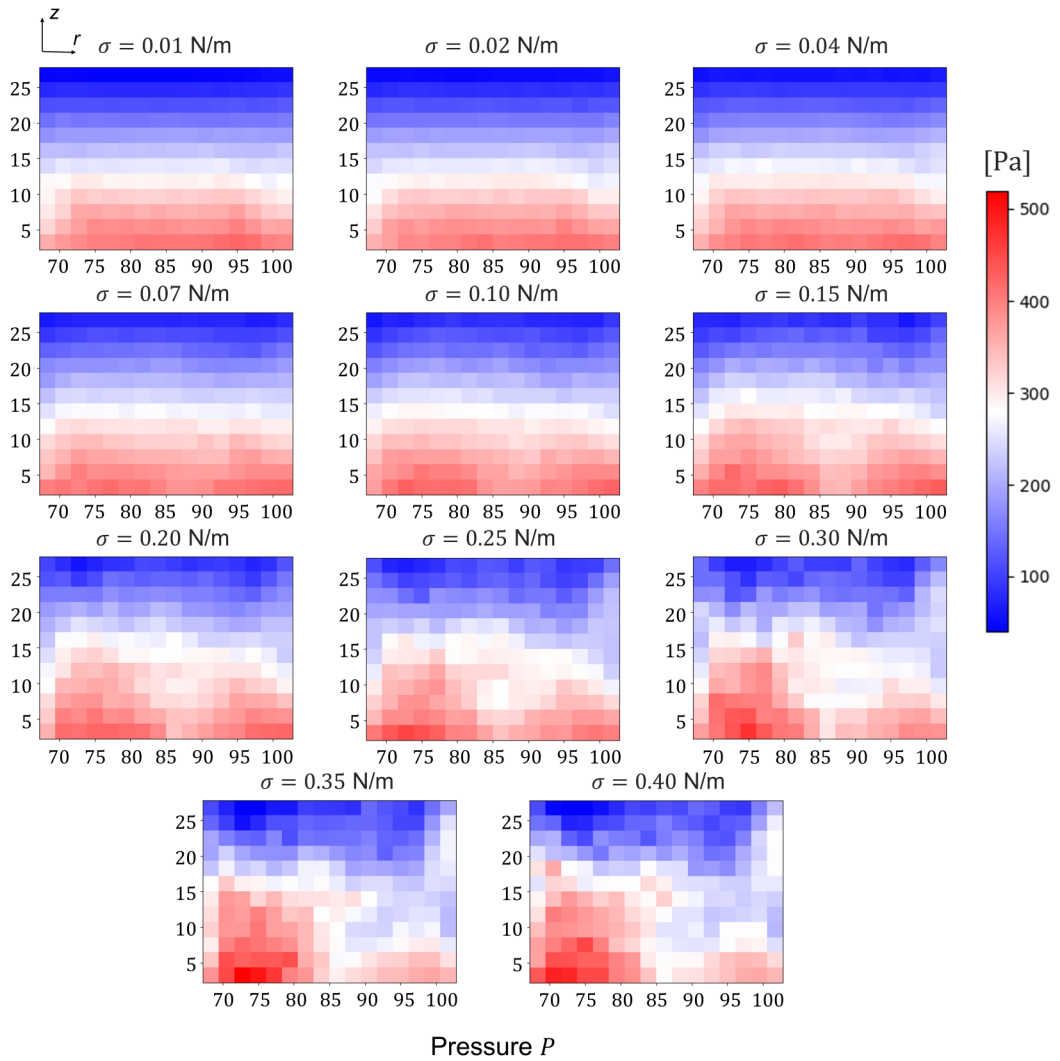


FIG. 23. Coarse-grained pressure in a cohesive split-bottom cell for different values of surface tension  $\sigma$  and a rotational rate  $\Omega = 0.16$  rad/s.

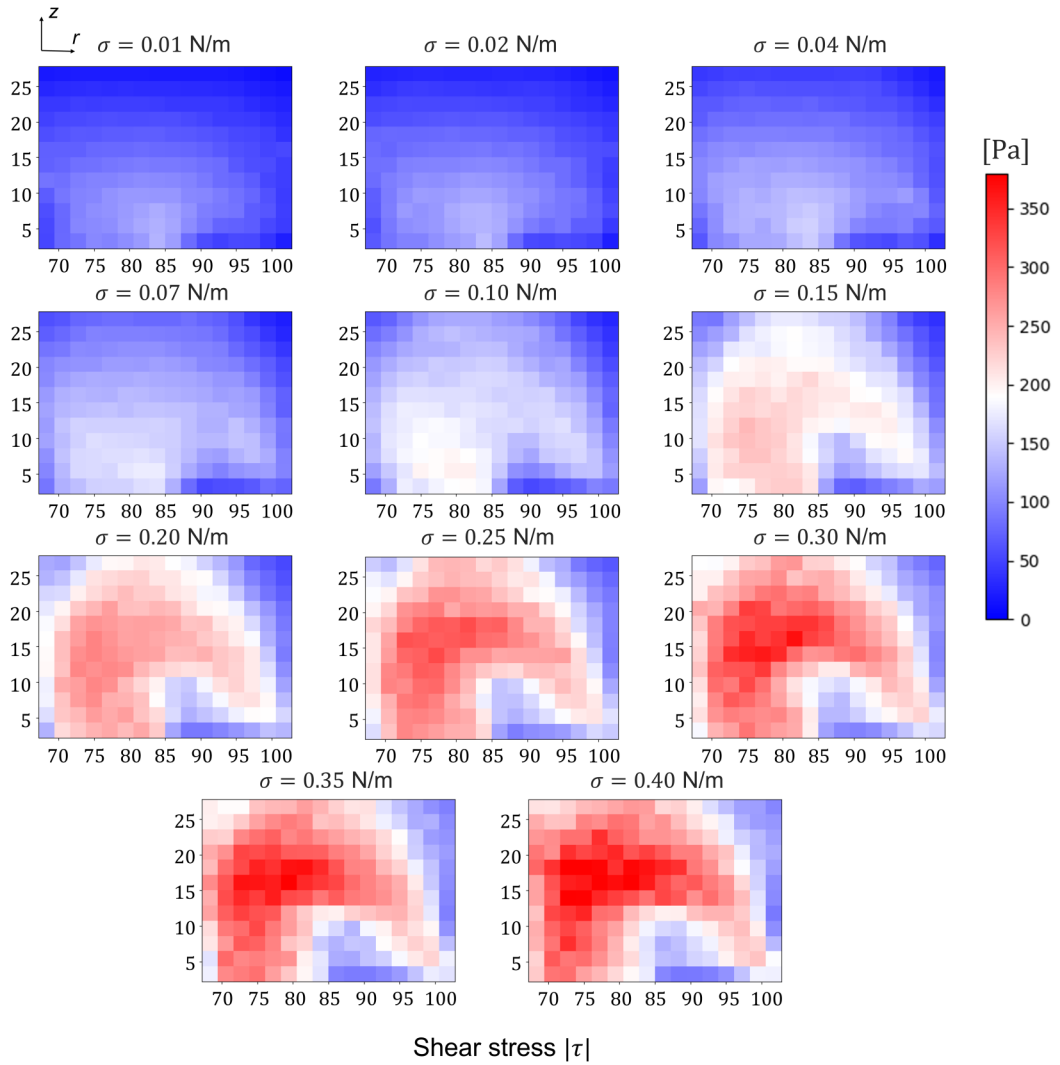


FIG. 24. Coarse-grained shear stress in a cohesive split-bottom cell for different values of surface tension  $\sigma$  and a rotational rate  $\Omega = 0.16$  rad/s.

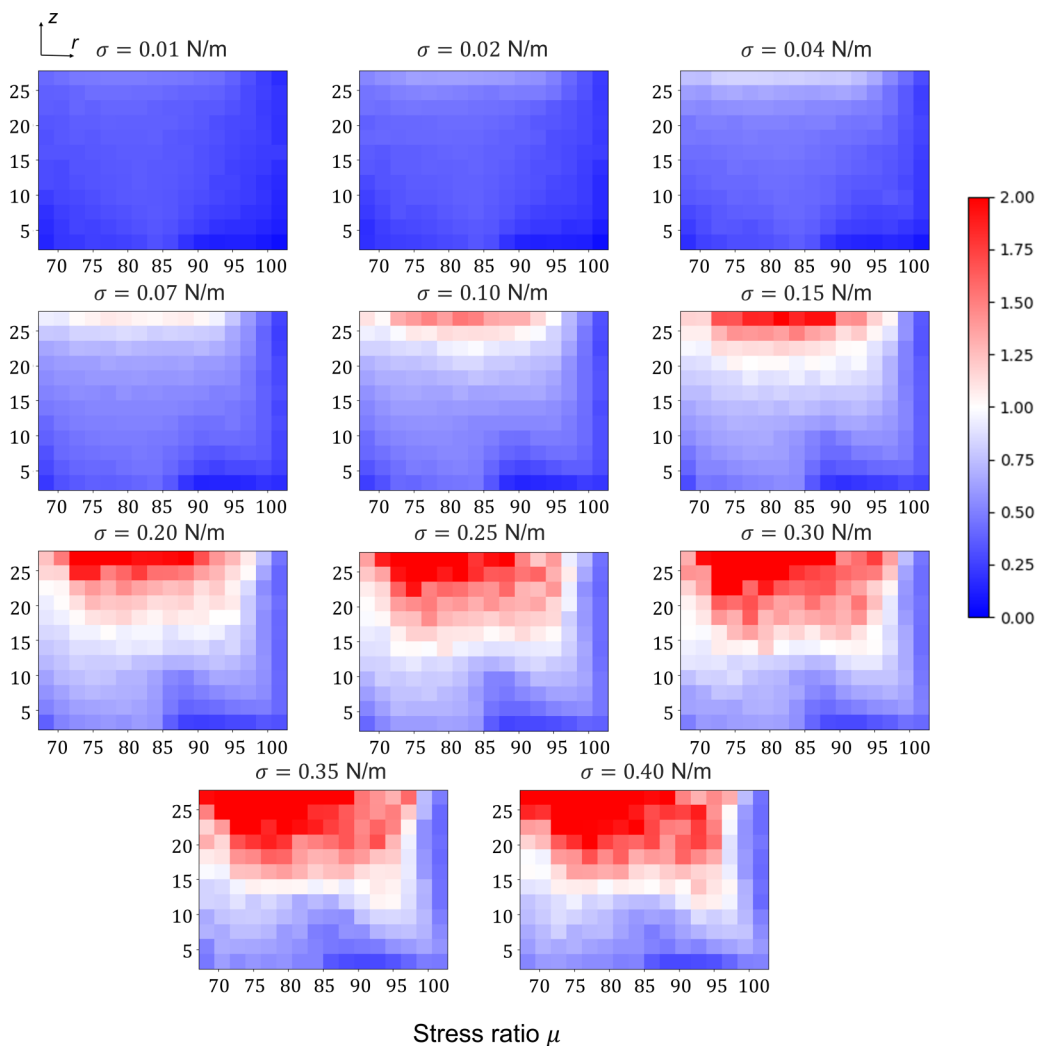


FIG. 25. Coarse-grained stress ratio in a cohesive split-bottom cell for different values of surface tension  $\sigma$  and a rotational rate  $\Omega = 0.16$  rad/s. The values of  $\mu$  have been capped at 2 to facilitate the comparisons.

- 
- [1] F. da Cruz, S. Emam, M. Prochnow, J. N. Roux, and F. Chevoir, Rheophysics of dense granular materials: discrete simulation of plane shear flows, *Phys. Rev. E* **72**, 021309 (2005).
- [2] P. Jop, Y. Forterre, and O. Pouliquen, A constitutive law for dense granular flows, *Nature (London)* **441**, 727 (2006).
- [3] L. Staron, P. Y. Lagrée, and S. Popinet, Continuum simulation of the discharge of the granular silo, *Eur. Phys. J. E* **37**, 5 (2014).
- [4] S. Dunatunga and K. Kamrin, Continuum modeling of projectile impact and penetration in dry granular media, *J. Mech. Phys. Solids* **100**, 45 (2017).
- [5] P. Y. Lagrée, L. Staron, and S. Popinet, The granular column collapse as a continuum: validity of a two-dimensional Navier-Stokes model with a  $\mu(i)$ -rheology, *J. Fluid Mech.* **686**, 378 (2011).
- [6] M. Bouzid, A. Izzet, M. Trulsson, E. Clément, P. Claudin, and B. Andreotti, Nonlocal rheology in dense granular flows, *Eur. Phys. J. E* **38**, 125 (2015).

- [7] K. Kamrin, Non-locality in granular flow: phenomenology and modeling approaches, *Front. Phys.* **7**, 116 (2019).
- [8] D. M. Mueth, Measurements of particle dynamics in slow, dense granular Couette flow, *Phys. Rev. E* **67**, 011304 (2003).
- [9] G. Chambon, J. Schmittbuhl, A. Corfdir, J. P. Vilotte, and S. Roux, Shear with comminution of a granular material: microscopic deformations outside the shear band, *Phys. Rev. E* **68**, 011304 (2003).
- [10] M. Depken, W. van Saarloos, and M. van Hecke, Continuum approach to wide shear zones in quasistatic granular matter, *Phys. Rev. E* **73**, 031302 (2006).
- [11] T. S. Komatsu, S. Inagaki, N. Nakagawa, and S. Nasuno, Creep Motion in a Granular Pile Exhibiting Steady Surface Flow, *Phys. Rev. Lett.* **86**, 1757 (2001).
- [12] K. Nichol, A. Zanin, R. Bastien, E. Wandersman, and M. van Hecke, Flow-Induced Agitations Create a Granular Fluid, *Phys. Rev. Lett.* **104**, 078302 (2010).
- [13] K. A. Reddy, Y. Forterre, and O. Pouliquen, Evidence of Mechanically Activated Processes in Slow Granular Flows, *Phys. Rev. Lett.* **106**, 108301 (2011).
- [14] G. MiDi, On dense granular flows, *Eur. Phys. J. E* **14**, 341 (2004).
- [15] S. Siavoshi, A. V. Orpe, and A. Kudrolli, Friction of a slider on a granular layer: nonmonotonic thickness dependence and effect of boundary conditions, *Phys. Rev. E* **73**, 010301(R) (2006).
- [16] X. Cheng, J. B. Lechman, A. Fernandez-Barbero, G. S. Grest, H. M. Jaeger, G. S. Karczmar, M. E. Möbius, and S. R. Nagel, Three-Dimensional Shear in Granular Flow, *Phys. Rev. Lett.* **96**, 038001 (2006).
- [17] D. Fenistein and M. van Hecke, Wide shear zones in granular bulk flow, *Nature (London)* **425**, 256 (2003).
- [18] J. Choi, A. Kudrolli, and M. Z. Bazant, Velocity profile of granular flows inside silos and hoppers, *J. Phys.: Condens. Matter* **17**, S2533 (2005).
- [19] I. Zuriguel, D. R. Parisi, R. C. Hidalgo, C. Lozano, A. Janda, P. A. Gago, J. P. Peralta, L. M. Ferrer, L. A. Pugnaloni, E. Clément, D. Maza, I. Pagonabarraga, and A. Garcimartín, Clogging transition of many-particle systems flowing through bottlenecks, *Sci. Rep.* **4**, 7324 (2015).
- [20] H. G. Sheldon and D. J. Durian, Granular discharge and clogging for tilted hoppers, *Granular Matter* **12**, 579 (2010).
- [21] O. Pouliquen, Scaling laws in granular flows down rough inclined planes, *Phys. Fluids* **11**, 542 (1999).
- [22] L. E. Silbert, L. J. W., and G. S. Grest, Granular flow down a rough inclined plane: transition between thin and thick piles, *Phys. Fluids* **15**, 1 (2003).
- [23] H.-B. Mühlhaus and I. Vardoulakis, The thickness of shear bands in granular materials, *Géotechnique* **37**, 271 (1987).
- [24] R. D. Borst, Simulation of strain localization: a reappraisal of the Cosserat continuum, *Eng. Comput.* **8**, 317 (1991).
- [25] J. T. Jenkins and S. B. Savage, A theory for the rapid flow of identical, smooth, nearly elastic, spherical particles, *J. Fluid Mech.* **130**, 187 (1983).
- [26] P. R. Nott, A non-local plasticity theory for slow granular flows, *EPJ Web Conf.* **140**, 11015 (2017).
- [27] O. Pouliquen and Y. Forterre, A non-local rheology for dense granular flows, *Philos. Trans. R. Soc. A* **367**, 5091 (2009).
- [28] I. S. Aranson and L. S. Tsimring, Continuum description of avalanches in granular media, *Phys. Rev. E* **64**, 020301 (2001).
- [29] C. Derec, A. Ajdari, and F. Lequeux, Rheology and aging: a simple approach, *Eur. Phys. J. E* **4**, 355 (2001).
- [30] D. Volfson, L. S. Tsimring, and I. S. Aranson, Order Parameter Description of Stationary Partially Fluidized Shear Granular Flows, *Phys. Rev. Lett.* **90**, 254301 (2003).
- [31] K. Kamrin and G. Koval, Nonlocal Constitutive Relation for Steady Granular Flow, *Phys. Rev. Lett.* **108**, 178301 (2012).
- [32] D. L. Henann and K. Kamrin, Continuum thermomechanics of the nonlocal granular rheology, *Int. J. Plast.* **60**, 145 (2014).
- [33] M. Bouzid, M. Trulsson, P. Claudin, E. Clément, and B. Andreotti, Nonlocal Rheology of Granular Flows across Yield Conditions, *Phys. Rev. Lett.* **111**, 238301 (2013).



- [34] D. L. Henann and K. Kamrin, A predictive, size-dependent continuum model for dense granular flows, *Proc. Natl. Acad. Sci. USA* **110**, 6730 (2013).
- [35] D. Liu and D. L. Henann, Non-local continuum modelling of steady, dense granular heap flows, *J. Fluid Mech.* **831**, 212 (2017).
- [36] D. L. Henann and K. Kamrin, Continuum Modeling of Secondary Rheology in Dense Granular Materials, *Phys. Rev. Lett.* **113**, 178001 (2014).
- [37] D. Liu and D. L. Henann, Size-dependence of the flow threshold in dense granular materials, *Soft Matter* **14**, 5294 (2018).
- [38] M. Bouzid, M. Trulsson, P. Claudin, E. Clément, and B. Andreotti, Microrheology to probe non-local effects in dense granular flows, *Europhys. Lett.* **109**, 24002 (2015).
- [39] C.-C. Lin and F.-L. Yang, Continuum simulation for regularized non-local  $\mu(i)$  model of dense granular flows, *J. Comput. Phys.* **420**, 109708 (2020).
- [40] M. Bouzid, M. Trulsson, A. Izzet, A. Favier de Coulomb, P. Claudin, E. Clément, and B. Andreotti, Non-local rheology of dense granular flows, *EPJ Web Conf.* **140**, 11013 (2017).
- [41] Z. Tang, T. A. Brzinski, M. Shearer, and K. E. Daniels, Nonlocal rheology of dense granular flow in annular shear experiments, *Soft Matter* **14**, 3040 (2018).
- [42] D. L. Henann and K. Kamrin, A finite element implementation of the nonlocal granular rheology, *Int. J. Numer. Methods. Eng.* **108**, 273 (2016).
- [43] Q. Zhang and K. Kamrin, Microscopic Description of the Granular Fluidity Field in Nonlocal Flow Modeling, *Phys. Rev. Lett.* **118**, 058001 (2017).
- [44] J. A. Robinson, D. J. Holland, and L. Fullard, Examination of the microscopic definition for granular fluidity, *Phys. Rev. Fluids* **6**, 044302 (2021).
- [45] J. Gaume, G. Chambon, and M. Naaïm, Microscopic Origin of Nonlocal Rheology in Dense Granular Materials, *Phys. Rev. Lett.* **125**, 188001 (2020).
- [46] S. Mandal, M. Nicolas, and O. Pouliquen, Rheology of Cohesive Granular Media: Shear Banding, Hysteresis, and Nonlocal Effects, *Phys. Rev. X* **11**, 021017 (2021).
- [47] J. Visser, An invited review—van der Waals and other cohesive forces affecting powder fluidization, *Powder Technol.* **58**, 1 (1989).
- [48] M. Mihajlovic, I. Roghair, and M. V. S. Annaland, On the numerical implementation of the van der waals force in soft-sphere discrete element models for gas-solid fluidization, *Chem. Eng. Sci.* **226**, 115794 (2020).
- [49] M. F. Al-Adel, D. A. Saville, and S. Sundaresan, The effect of static electrification on gas-solid flows in vertical risers, *Ind. Eng. Chem. Res.* **41**, 6224 (2002).
- [50] K. Kuwagi, T. Mikami, and M. Horio, Numerical simulation of metallic solid bridging particles in a fluidized bed at high temperature, *Powder Technol.* **109**, 27 (2000).
- [51] C. D. Willett, M. J. Adams, S. A. Johnson, and J. P. K Seville, Capillary bridges between two spherical bodies, *Langmuir* **16**, 9396 (2000).
- [52] K. Washino, E. L. Chan, T. Matsumoto, S. Hashino, T. Tsuji, and T. Tanaka, Normal viscous force of pendular liquid bridge between two relatively moving particles, *J. Colloid Interface Sci.* **494**, 255 (2017).
- [53] K. Washino, E. L. Chan, H. Midou, T. Tsuji, and T. Tanaka, Tangential viscous force models for pendular liquid bridge of Newtonian fluid between moving particles, *Chem. Eng. Sci.* **174**, 365 (2017).
- [54] D. Fenistein, J. W. van de Meent, and M. van Hecke, Universal and Wide Shear Zones in Granular Bulk Flow, *Phys. Rev. Lett.* **92**, 094301 (2004).
- [55] S. Luding, The effect of friction on wide shear bands, *Part. Sci. Technol.* **26**, 33 (2007).
- [56] S. Roy, S. Luding, and T. Weinhart, A general(ized) local rheology for wet granular materials, *New J. Phys.* **19**, 043014 (2017).
- [57] J. A. Dijkstra and M. van Hecke, Granular flows in split-bottom geometries, *Soft Matter* **6**, 2901 (2010).
- [58] P. Jop, Hydrodynamic modeling of granular flows in a modified Couette cell, *Phys. Rev. E* **77**, 032301 (2008).
- [59] J. Goyon, A. Colin, G. Ovarlez, A. Ajdari, and L. Bocquet, Spatial cooperativity in soft glassy flows, *Nature (London)* **454**, 84 (2008).

- [60] L. Bocquet, A. Colin, and A. Ajdari, Kinetic Theory of Plastic Flow in Soft Glassy Materials, *Phys. Rev. Lett.* **103**, 036001 (2009).
- [61] S. Kim and K. Kamrin, Power-Law Scaling in Granular Rheology across Flow Geometries, *Phys. Rev. Lett.* **125**, 088002 (2020).
- [62] P. A. Cundall and O. D. L. Strack, A discrete numerical model for granular assemblies, *Géotechnique* **29**, 47 (1979).
- [63] W. Goldsmith, *Impact: The Theory and Physical Behavior of Colliding Solids* (Edward Arnold, London, UK, 1960).
- [64] R. D. Mindlin, Compliance of elastic bodies in contact, *J. Appl. Mech.* **16**, 259 (1949).
- [65] G. Lian, C. Thornton, and M. J. Adams, A theoretical study of the liquid bridge forces between two rigid spherical bodies, *J. Colloid Interface Sci.* **161**, 138 (1993).
- [66] G. Lian, C. Thornton, and M. J. Adams, Discrete particle simulation of agglomerate impact coalescence, *Chem. Eng. Sci.* **53**, 3381 (1998).
- [67] Y. Muguruma, T. Tanaka, and Y. Tsuji, Numerical simulation of particulate flow with liquid bridge between particles (simulation of centrifugal tumbling granulator), *Powder Technol.* **109**, 49 (2000).
- [68] T. Mikami, H. Kamiya, and M. Horio, Numerical simulation of cohesive powder behavior in a fluidized bed, *Chem. Eng. Sci.* **53**, 1927 (1998).
- [69] Y. I. Rabinovich, M. S. Esayanur, and B. M. Moudgil, Capillary forces between two spheres with fixed volume liquid bridge: theory and experiment, *Langmuir* **21**, 10992 (2005).
- [70] P. Y. Liu, R. Y. Yang, and A. B. Yu, Dynamics of wet particles in rotating drums: effect of liquid surface tension, *Phys. Fluids* **23**, 013304 (2011).
- [71] E. Hairer, C. Lubich, and G. Wanner, *Geometric Numerical Integration: Structure-Preserving Algorithms for Ordinary Differential Equations* (Springer-Verlag, New York, 2002).
- [72] Y. Li, Y. Xu, and C. Thornton, A comparison of discrete element simulations and experiments for “sandpiles” composed of spherical particles, *Powder Technol.* **160**, 219 (2005).
- [73] M. Lätzel, S. Luding, and H. J. Herrmann, Macroscopic material properties from quasistatic, microscopic simulations of a two-dimensional shear-cell, *Granular Matter* **2**, 123 (2000).
- [74] S. Luding, Constitutive relations for the shear band evolution in granular matter under large strain, *Particuology* **6**, 501 (2008).
- [75] A. Singh, V. Magnanimo, K. Saitoh, and S. Luding, The role of gravity or pressure and contact stiffness in granular rheology, *New J. Phys.* **17**, 043028 (2015).
- [76] S. Rüdiger, A. Gladky, F. Uhlig, and S. Luding, Rheology of weakly wetted granular materials: a comparison of experimental and numerical data, *Granular Matter* **15**, 455 (2013).
- [77] A. Singh, V. Magnanimo, K. Saitoh, and S. Luding, Effect of cohesion on shear banding in quasistatic granular materials, *Phys. Rev. E* **90**, 022202 (2014).
- [78] Q. Huang, H. Zhang, and J. Zhu, Experimental study on fluidization of fine powders in rotating drums with various wall friction and baffled rotating drums, *Chem. Eng. Sci.* **64**, 2234 (2009).
- [79] R. Maione, S. Kiesgen De Richter, G. Mauviel, and G. Wild, DEM investigation of granular flow and binary mixture segregation in a rotating tumbler: influence of particle shape and internal baffles, *Powder Technol.* **286**, 732 (2015).
- [80] F. Charru, E. Larrieu, J.-B. Dupont, and R. Zenit, Motion of a particle near a rough wall in a viscous shear flows, *J. Fluid Mech.* **570**, 431 (2007).
- [81] J. T. Jenkins and M. W. Richman, Boundary conditions for plane flows of smooth, nearly elastic, circular disks, *J. Fluid Mech.* **171**, 53 (1986).
- [82] M.-L. Tan and I. Goldhirsch, Rapid Granular Flows as Mesoscopic Systems, *Phys. Rev. Lett.* **81**, 3022 (1998).
- [83] B. J. Glasser and I. Goldhirsch, Scale dependence, correlations, and fluctuations of stresses in rapid granular flows, *Phys. Fluids* **13**, 407 (2001).
- [84] C. Goldenberg, A. P. F. Atman, P. Claudin, G. Combe, and I. Goldhirsch, Scale Separation in Granular Packings: Stress Plateaus and Fluctuations, *Phys. Rev. Lett.* **96**, 168001 (2006).
- [85] J. Török, T. Unger, J. Kertész, and D. E. Wolf, Shear zones in granular materials: optimization in a self-organized random potential, *Phys. Rev. E* **75**, 011305 (2007).

- [86] M. Kobayakawa, S. Miyai, T. Tsuji, and T. Tanaka, Local dilation and compaction of granular materials induced by plate drag, *Phys. Rev. E* **98**, 052907 (2018).
- [87] S. T. Nase, W. L. Vargas, A. A. Abatan, and J. J. McCarthy, Discrete characterization tools for cohesive granular material, *Powder Technol.* **116**, 214 (2001).
- [88] P. G. Rognon, J.-N. Roux, M. Naaim, and F. Chevoir, Dense flows of cohesive granular materials, *J. Fluid Mech.* **596**, 21 (2008).
- [89] M. Macaulay and P. Rognon, Viscosity of cohesive granular flows, *Soft Matter* **17**, 165 (2021).
- [90] S. Roy, A. Singh, S. Luding, and T. Weinhart, Micro-macro transition and simplified contact models for wet granular materials, *Comp. Part. Mech.* **3**, 449 (2016).
- [91] A. Schofield and P. Wroth, *Critical State Soil Mechanics* (McGraw-Hill, London, 1968).
- [92] A. Ries, D. E. Wolf, and T. Unger, Shear zones in granular media: three-dimensional contact dynamics simulation, *Phys. Rev. E* **76**, 051301 (2007).
- [93] B. Szabó, J. Török, E. Somfai, S. Wegner, R. Stannarius, A. Böse, G. Rose, F. Angenstein, and T. Börzsönyi, Evolution of shear zones in granular materials, *Phys. Rev. E* **90**, 032205 (2014).
- [94] W. Nan, M. Pasha, and M. Ghadiri, Rheology of a dense granular bed penetrated by a rotating impeller, *Powder Technol.* **386**, 60 (2021).
- [95] C. K. K. Lun, S. B. Savage, and D. J. Jeffrey, Kinetic theories for granular flow: inelastic particles in Couette flow and slightly inelastic particles in a general flowfield, *J. Fluid Mech.* **140**, 223 (1984).
- [96] N. F. Carnahan and K. E. Starling, Equation of state for nonattracting rigid spheres, *J. Chem. Phys.* **51**, 635 (1969).
- [97] Y. Tsuji, T. Tanaka, and T. Ishida, Lagrangian numerical simulation of plug flow of cohesionless particles in a horizontal pipe, *Powder Technol.* **71**, 239 (1992).
- [98] D. Faroux, K. Washino, T. Tsuji, and T. Tanaka, A FVM implementation and validation of non-local modeling for single- and two-phase granular flows, *Comput. Part. Mech.* (2022), doi:10.1007/s40571-021-00455-5.
- [99] D. Faroux, K. Washino, T. Tsuji, and T. Tanaka, 3D implementation and validation of VOF-coupled non-local granular rheology, *Granular Matter* **24**, 52 (2022).